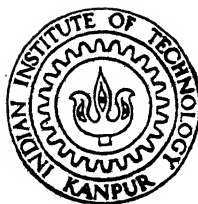# STUDY OF 1 MeV Kr^{++} ION INDUCED MIXING AT THE INTERFACE OF TELLURIUM THIN FILMS EVAPORATED ON ZINC SUBSTRATES

by

RANJIT D. PRADHAN

MATERIALS SCIENCE PROGRAMME

INDIAN INSTITUTE OF TECHNOLOGY KANPUR

MAY, 1991

STUDY OF 1 MeV Kr++ ION INDUCED MIXING AT THE INTERFACE OF TELLURIUM THIN FILMS EVAPORATED ON ZINC SUBSTRATES

A thesis submitted
in partial Fulfilment of the Requirements
for the degree of
Master of Technology

by
Ranjit D. Pradhan

To

Materials Science Programme

INDIAN INSTITUTE OF TECHNOLOGY, KANPUR

MAY, 1991

MSP- 1991- M - PRA - STU

Dedicated

To

My Parents

ABSTRACT

This thesis reports, for the first time, the investigation of Ion Beam Mixing in the zinc-tellurium bilayer system. Thin films of tellurium in the thickness range 1800 to 3500 angstroms were deposited on chemically etched zinc substrates. The bilayer configuration was irradiated with 1 MeV Kr^{++} ions in the dose range of 6.7×10^{15} to 4.8×10^{16} atoms / cm^2. These irradiated samples were analysed by Rutherford Backscattering spectroscopy, Scanning Electron Microscopy and X-Ray Diffraction techniques in order to investigate the depth distribution of Te and Zn, surface topography and phase formation after Ion Beam Mixing. The study of the concentration distribution (mixed amount of Te in Zn and vice versa) as a function of Kr irradiation dose shows $\phi^{1/2}$ dependence which is indicative of the dominance of the mechanism which involves delayed processes viz radiation enhanced diffusion. The formation of ZnTe cubic phase has been confirmed by the X-Ray diffraction measurement above the irradiation fluence of 4×10^{16} Kr ions / cm^2 on samples with tellurium thickness of 3200 Å.
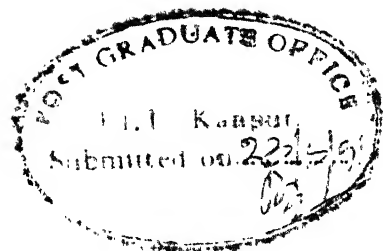
CERTIFICATE

It is certified that the work contained in the thesis entitled "STUDY OF 1 MeV Kr^{++} ION INDUCED MIXING AT THE INTERFACE OF TELLURIUM THIN FILMS EVAPORATED ON ZINC SUBSTRATES" by "RANJIT D.PRADHAN" has been carried out under our supervision and that this work has not been submitted elsewhere for a degree.

Prof. K.N. Rai

Materials Science Programme,

I.I.T. Kanpur.

23 May 1991.

Dr. V.N. Kulkarni

Department of Physics,

I.I.T. Kanpur.

23 May 1991.

ACKNOWLEDGEMENTS

C O N T E N T S

LIST OF FIGURES

CHAPTER 1

INTRODUCTION

The study of surfaces of materials has received considerable attention over the last few decades. In areas like semiconductor devices the predominance of surface phenomena is most easily seen. The electrical behaviour of the outer few microns of the semiconductor is crucial to the operation of the device. In the study and preparation of corrosion resistant materials, only their surface (the outer few microns) is of interest. The same applies to wear and tear of metals, alloys and other materials.

In other instances, it is possible to enhance the usability of bulk materials by suitably tailoring their surfaces [1]. On application of loads on these materials, stress concentrations occur at the crack tips and the failure of the material results due to the propagation of cracks from the surface. Thus the nature of the surface is intimately linked with many bulk mechanical properties. Further, suitable modification of the surface is, many a times, more economical than modifying the bulk material, to achieve the same effect.

One of the direct ways of tailoring surface properties is by ion implantation [1,2,3]. It involves impregnating the material surface by injecting accelerated impurity ions. Their acquired kinetic energy carries them into the material surface and the depth at which they settle down

depends on their incident energy. Table 1.1 presents the pros and cons of ion implantation as a surface engineering tool. The constraints on the choice of the ion, successive implantation of various types of ions and the selectivity of the region to be modified are minor and high temperature treatment is not always necessary.

Ion implantation has been used extensively in semiconductors [3]. However many new areas of research suggest its applicability in other areas. An example is the successful use of 150 Kev cromium implantation [2] in U.S. naval bearings, to increase their corrosion resistance, without deteriorating their mechanical performance. In semiconductors, applications have emerged for ion implantation beyond 150 Kev energies [4,5]. Figure 1.1 summarizes the typical applications of high energy ion implantation [4]. The rectangular region on the left of the Figure, shown in the dashed lines, encloses the dose and energy combinations possible at the Central Nuclear Facility.

One of the limitations of ion implantation has been the problem of sputtering or ion induced erosion of the bombarded surface. This places an upper limit to the maximum concentration of impurities, in the host, attainable by implantation and is roughly given by r/s [6]. Here r is called the preferential sputtering factor which confines itself to values between 0.5 and 2.0. S is the sputtering yield which is defined as the total number of target atoms sputtered per incident projectile/impurity ion. S could be as high as 20. For example, in the case of 150 Kev Au implantation into Fe, the value for r is unity and S equals 4.4. This yields a maximum Au concentration in Fe of a little over 25 % . However, for

TABLE - 1.1

ADVANTAGES

1. Controllable addition of impurities.
2. Ion energy control of ion range.
3. Multienergy implants offer a depth tailored profile.
4. Small lateral spread of implanted ions.
5. Ion ranges are not sensitive to dislocations, unlike the thermal diffusion lengths.
6. Implanted species need not be in thermal equilibrium. Hence the solid solubility limit can be exceeded.
7. Control of processing temperature.
8. Formation of buried layers.
9. Solid phase epitaxy in conjunction with pulse annealing over selected region possible.
10. Amorphization with relatively low doses of heavy ions.
11. High vacuum cleanliness. Therefore suitable for the processing of ultra-pure materials.

DISADVANTAGES

1. Line of sight process.
2. Shallow ion penetrations.
3. Relatively expensive equipment and processing costs.
4. Radiation damage (present annealing techniques can "repair" this damage to a certain extent and in certain cases like amorphization the radiation damage may turn out to be useful).
5. Problem of sputtering.

simillar Au implantation into Cu, the maximum achievable concentration is about 5 % . This is due to the S value being 20 in the case of Cu [7].

The above mentioned limitation, caused by the phenomenon of sputtering, can be circumvented by depositing a thin film of impurity A on the host substrate B and bombarding this bilayer configuration with energetic heavy ions [6], especially inert gas ions. The dynamical processes, triggered as the ion passes through the bilayer, have been found to induce mixing of atoms of A with those of B, at the interface. This variation of ion implantation is commonly known as "Ion Induced Atomic Mixing" or simply "Ion Beam Mixing." In most cases ion beam mixing has been observed to have no upper bound to the concentration of atoms of A in B [2].

Many exotic applications of this technique have arisen in recent years. They include silicide formation, synthesis of metastable and amorphous alloys and applications in improvement of thin film adhesion to the substrates under the influence of ion induced mixing. For example, Galuska [28] has reported the adhesion enhancement of Ni films on polyesters, using Kr^+ implantation. Another recent study by Hohmuth et.al. [29] involved fabrication of a Y-Ba-Cu Oxide film by ion induced mixing of multilayers of Y,Ba and Cu followed by post irradiation oxygen annealing .

I). FUNDAMENTAL ION BEAM MIXING MECHANISMS :-

It is now appropriate to briefly review the basic mechanisms through which ion beam mixing results [2,8]. These mechanisms can be categorised on the basis of the time scales

over which the various processes involved are predominant. This classification is presented in Table 1.2.

1) PROMPT REGIME (RECOIL MIXING) :-

As shown in Table 1.2, the prompt regime extends over a period of about 10 picoseconds following the entry of the ion beam into the target. This regime includes the following basic processes :-

i) PRIMARY RECOIL MIXING [8.9] :- This mixing mechanism is at play during first few picoseconds following the impact of the energetic ion on the target atoms. The primary recoils lose their energy via electronic exitations and sometimes due to violent collisions with the target atoms. Some of the primary recoils travel relatively long distances in the solid, gradually dissipating their energy to electronic exitations and finally come to rest deep below the surface. Consequently, long tails appear in the concentration profiles of the impurities. These long tails are definite signatures of the primary recoil mixing process.

ii) CASCADE MIXING MECHANISM [2,8,10,11] :- Just after the primary recoil mixing processes die down, cascades begin to develop along the path of the projectile and the primary recoil paths. Figure 1.2 shows a particularly violent collision cascade known as a displacement spike [12]. Cascades result in widespread lattice damage. A heavy ion of 100 KeV, for example, incident on silicon can displace upto a thousand atoms. Such individual cascades result in damaged zones of several tens of angstroms.

One important point, regarding cascades, needs to be added. The probability of individual cascades overlapping in

TABLE - 1.2

BASIC   PROCESSES

PROMPT   PROCESSES

(RECOIL   MIXING)
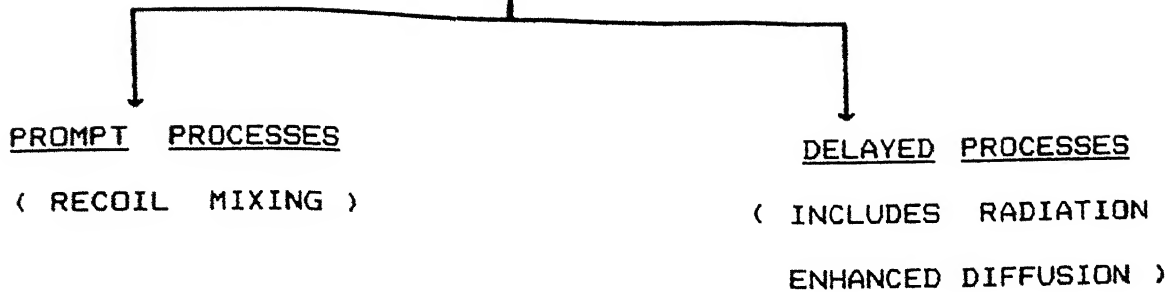
TIME SCALE :-
FROM 0.1 TO 10.0 PICOSECONDS
FOLLOWING   THE IMPACT OF THE
IMPACT OF   THE ENERGETIC ION
ON THE TARGET.

(Temperature independent

phenomena)

DELAYED PROCESSES

(INCLUDES   RADIATION

ENHANCED DIFFUSION)

TIME SCALES :-
FROM 10.0 PICOSECONDS
TO ONE SECOND OR MORE.

(Dependent on sample

temperature.)

PRIMARY   RECOIL   MIXING .
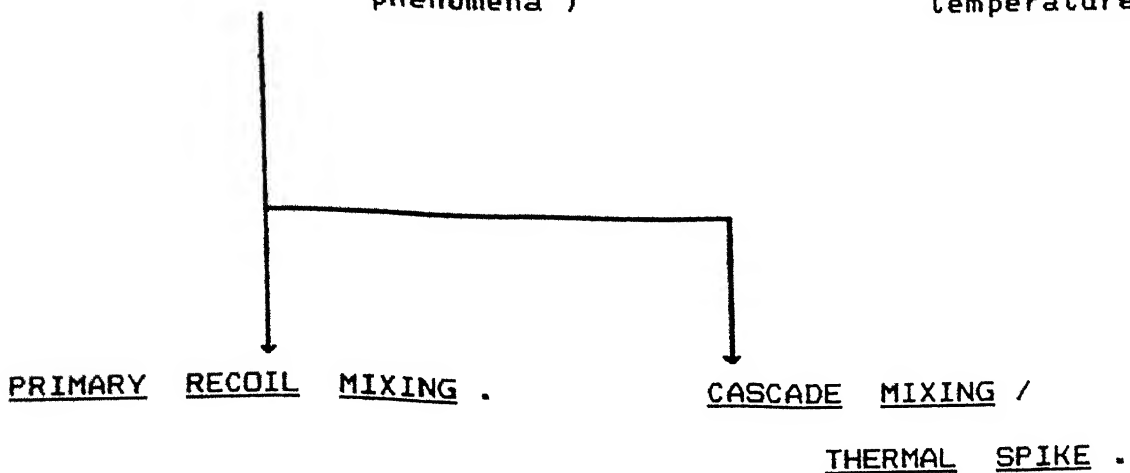
TIME SCALE :-
FROM 0.1 TO 1.0
PICOSECONDS
    Primary recoils in the
forward direction carried
deep into the target.

CASCADE   MIXING /

THERMAL   SPIKE .

FROM 1.0 TO 10.0
PICOSECONDS
    Widespread lattice
damage over a few tens of
Å .

space (at a fixed time) is negligible [2] . For example, at a current density of 1 $\mu A/cm^2$, successive cascades of about 20 Å dimensions occur over a given region at roughly one second intervals while the individual cascade quenching times are of the order of picoseconds. The region over which the cascade exists may be considered to be locally melted giving quenching rates of the order of 10^{14} $^oK/sec$.

Secondly, since each cascade extends over a region of about 20 Å diameter, it is reasonable to expect only 20 Å pockets of modified region, at very low doses. The minimum dose at which these pockets begin to merge in a continuous fashion can be estimated. Assuming the area of each cascade to be of the order of $10^{-14} cm^2$, this threshold dose turns out to be of the order of $10^{+14} ions/cm^2$. Beyond this threshold one can expect the modified interface to be continuous.

In the prompt regime the mixed amount is linearly dependent on the ion dose ϕ . The origin of this dependence is the non-overlap of the collision cascades. Prompt processes are also temperature independent. The study of the prompt regime needs to be done at low temperatures, to supress the delayed effects. The ϕ dependence has been observed in a large number of systems at reduced temperatures. Some of them are systems like Ge-Si, Ge-Al [13], Ni-Au [14], and many others [8].

2) DELAYED REGIME :-

This mechanism takes over after the prompt processes get quenched. The quenching of the prompt processes leaves behind a multitude of defects like Frenkel pairs [8]. Enhancement in the diffusion process results due to the motion

of these radiation induced defects, stimulated by the residual agitation of the lattice by the energetic ion. This process is commonly referred to as "Radiation Enhanced Diffusion" [15,16,17] and depends on the conditions under which the sample was irradiated. This process is limited by the recombination rate of the vacancy-interstitial pairs. It is therefore referred to as a rate limited process.

The delayed processes are temperature dependent and the mixed amounts vary as $\phi^{1/2}$ when this mechanism becomes dominant.

II) SAMPLE CONFIGURATIONS FOR THE INVESTIGATION OF ION BEAM MIXING :-

In the study of ion beam mixing three major sample configurations are employed. they are :-

    i) Marker configuration,

    ii) Bilayer configuration,

and   iii) Multilayer configuration.

i) MARKER SYSTEMS :-

Marker systems [8] are usually the simplest ones for studying ion beam mixing. A marker, shown in Figure 1.3(a), is a thin layer, typically about 10 Å thick, buried in an otherwise homogeneous medium. Their concentration profiles, prior to bombardment are in the form of step functions. The profile quickly spreads following ion irradiation. The amount of mixing is quantified by the irradiation induced increase in the standard deviation σ^2. The effective diffusion lengths $(Dt)^{1/2}$ are given by Equation 1.1.

$$Dt = \sigma^2/2 \qquad\qquad (1.1).$$

where D is the effective diffusion coefficient and t is the time over which the diffusion process is considered. The analysis of the sample is usually done by Rutherford Backscattering Spectrometry (RBS) (Appendix B).

Marker experiments are performed mainly to understand the basic processes influencing ion induced atomic mixing. The quick dispersion of the marker layer over a wide region minimizes the effect of chemical driving forces. Many systems have been studied using the marker configuration, for example studies with markers Au, Pt, Sb [18,19], Sn [20] in silicon, etc.

ii) BILAYER CONFIGURATION :-

Bilayer configurations involve two non-overlapping layers before ion bombardment. Both configurations shown in Figure 1.3(b) fall in this class. Each layer could be several hundred angstroms or more. This means that, for normal irradiation doses, the supply of the two components is "virually" infinte. The interest here is focused around formation of binary phases of any composition in addition to understanding the basic processes at play around the interface. In many experiments, a small long range component of mixing, has been observed [21,22,23]. The component, as stated earlier, has been identified with the recoil mixing process. The systems studied under the bilayer configuration, like the marker systems, form a very large class [8]. Some examples are Al/Cu (copper being the top layer) [21], Au/Al [24] in which Au_2Al and $AuAl_2$ phase formations were observed, <Si>/Ni [25] where nickel silicide Ni_2Si phases were identified, and many other systems.

iii) MULTILAYER CONFIGURATION :-

Multilayer configurations, shown in Figure 1.3(c), are mainly important from the point of view of metastable and amorphous alloy formations. To achieve intermixing in immiscible systems, one can deposit multiple thin layers [26,27] and then bombard the multilayer structure with inert gas ions. The required composition can be established by adjusting the relative thicknesses of the films in the multilayer structure. One of the important features offered by this configuration is the limited supply of materials from each film in the multilayer structure.

The amorphization mechanisms have not been fully understood. Although atomic collisions trigger the mass transport, diffusion processes are also important. Very dense collision cascades (spikes) are believed to govern amorphization in many binary systems. In the case of metal-metal systems the resulting alloy may be expected to be amorphous if the constituent metals possess different crystal structures, irrespective of their atomic sizes and electronegativities [30]. This rule has been refered to as the "structural difference rule." There have been indications that the rule can be extended to metal-semiconductor systems. However, even in metal-metal systems, some exceptions to this rule exist. They include Au(f.c.c.)-Fe(b.c.c.) [26], Co(h.c.p.)-Cu(f.c.c.) [27], and Co(h.c.p.)-Ag(f.c.c.) [27]. These systems do not amorphize under ion beam mixing. Other criteria for amorphization to occur include considerations of the ratio of the atomic radii and the heat of mixing ΔH for the system [31]. Multilayer structures have also been used to

obtain many stoichiometric compounds. For example, amorphous Mo-Ru superconducting films have been prepared by this technique [32]. A recent study included the preparation of Y-Ba-Cu Oxide films by ion beam mixing [29].

III) CLASSES OF MATERIALS STUDIED UNDER ION BEAM MIXING :-

Silicides are of condiderable technological importance, especially in microelectronics where they are used as interconnects in integrated circuits. Silicides were the first systems to be studied exhaustively under ion beam mixing [8,18,34,35]. Platinum silicide studies were the first to be reported, in detail, as early as 1979 [34]. Other studies include marker experiments with Si-Au (Au being the marker) [18], Si-Ni [18,19], Pd-Si [18], and bilayer experiments on <Si>/Ni (Ni being the top layer on single crystalline Si) [25], <Si>/Cr [24], <Si>/Nb [36], etc.

The next important class of systems studied under ion induced mixing were the metal metal systems. In the first half of the eighties more than 30 binary metal systems were studied using multilayer configurations. A great number of metastable alloys, including various amorphous alloys, were obtained, many of which are not obtainable by traditional means [37] like splat cooling or any of the melt quenching techniques. These systems include Ag-Co, Cu-Co [27], Al-Au, Al-Co, Co-Ti, Ni-Ti [38], Mo-Ru [32], etc.

In the last five years interest has centered around metal-semiconductor, ceramic-metal systems and systems involving insulators like polymers. Some studies were reported for ion beam mixing in gallium arsenide [39,40,41,42]. For

example, Johnson et.al. [39] reported work on Sn doping in GaAs by ion beam mixing. They found that the maximum achievable concentration of Sn in GaAs by ion beam mixing at room temperature far exceeded the maximum limit of 2×10^{21} cm^{-3} in the case of laser mixing. However as compared to the silicides and the metal systems the attention received by semiconductors is sparse. Recently many metal-insulator couples have been investigated, especially in connection with adhesion improvement which is particularly useful in microelectronics [43,44]. Metal-SiO$_2$ systems have also received attention in the literature [45,46,47]. An example is the study of Fe-SiO$_2$ interfaces under ion beam mixing [47,48,49]. An example of the polymer-metal system is Galuska's study [28] of adhesion of Ni films on polyester under ion induced mixing, as mentioned earlier.

IV) THE ZINC-TELLURIUM COUPLE :-

The system chosen in this thesis work is the interface of tellurium thin films on zinc substrates. This system was found to be interesting as it is a case of a metal-metal system which can form a zinc telluride cubic phase. One of the possible application of ZnTe compound thin films is in the high efficiency tandem solar cell structures which utilize the large band gap of (Cd, Zn)Te alloys, in which ZnTe forms the transparent back contact [51]. Both the metals exhibit hexagonal structures in their bulk form. The zinc-tellurium phase diagram shows a stable ZnTe zincblende structure at 50 atomic percent of zinc. Cubic ZnTe is a group II-VI compound semiconductor (room temperature band gap of 2.26

eV). This was one of the motivating factors, in addition to fundamental academic interests, behind the choice of this system.

Kimmerle et.al. have reported preparation of zinc telluride thin films by evaporation of zinc telluride compound on heated substrates [52]. Preparation of ZnTe compound films has also been attempted by electrodeposition of Zn and Te followed by thermal annealing [51]. Zinc telluride thin film preparation by ion beam mixing techniques has not yet been attempted elsewhere. It may not be necessary to resort to high temperature treatment to obtain the required result. Further, is also offers lateral selectivity of the modification region, in addition to all the other advantages of ion implantation listed in Table 1.1.

The bilayer configuration has been employed in this study, where the tellurium supply for ion beam mixing is "nearly" infinite while the zinc supply is truely infinite. The experimental procedure is detailed in chapter 2. All ion beam mixing work in this thesis constitutes a room temperature study. The major surface analysis technique employed is Rutheford Backscattering Spectrometry (RBS) which has become indispensible for the study of surface modifications under ion bombardment. RBS has been supplemented by Scanning Electron Microscopy (SEM) and X-Ray Diffraction (XRD) analysis of the samples.

The TRIM88 programs were utilised in order to simulate the motion of energetic Kr ions in the zinc-Tellurium structure. The choice of the sample structure was also based on the preliminary information provided, by the TRIM program, on

the ion ranges and energy deposition of 1 MeV krypton ions in the top tellurium layer.

The analysis of the experimental results and the information extracted about the mixing process at the zinc-tellurium interface is presented in chapter 3.

This thesis terminates with the conclusions drawn on the basis of the experimental findings and possible extensions of this work.

.

CHAPTER 2

EXPERIMENTAL

2.1. SAMPLE PREPARATION

2.1.1 SUBSTRATE PREPARATION

Chemically polished zinc foils were used as substrates for tellurium thin film deposition. These zinc foils were obtained by cold rolling pieces of a 99.99 % pure zinc sheet supplied by Goodfellow Metals Ltd. U.K. The foils were mechanically polished using 3/0 and 4/0 grade polishing papers to smoothen out the undulations left on their surface by the rolling machine. They were then chemically etched in a 10 % solution of nitric acid. The foils were briefly dipped in the etchant for about half a minute using a tweezer after which they were quickly imersed in distilled water to prevent further etching. This process was repeated several times till a sufficiently good surface finish was achieved.

2.1.2. THIN FILM DEPOSITION

Tellurium thin film deposition was carried out on the zinc substrates by thermal evaporation of tellurium in a vacuum of about 5×10^{-6} Torr. Figure 2.1 shows the thin film deposition unit used. Initially the mass of tellurium M required to obtain a film of thickness t was calculated on the

basis of the following relation

$$M = 2 \pi R^2 \cdot \rho \cdot t \qquad\qquad (2.1).$$

where ρ is the bulk density of the material to be evaporated and R is the distance between the substrates and the evaporation boat. This mass M of tellurium was taken in a tantalum boat and evaporated on aluminium substrates. The deposited films were analysed by the Rutherford Backscattering technique (RBS) to acertain their thicknesses. It was found that the thickness obtained by the use of Equation 1 varied by as much as 25 % . This is due to the non-adherence to the perfect 2π geometry assumed in arriving at Equation 2.1. By a few such trial depositions followed by their RBS (Appendix-B) analysis a proper correction factor for the tantalum boat and evaporation geometry was fixed. The optimum distance between the boat and the zinc substrates was found to be about 10 cms. The mass of tellurium taken for evaporation varied between 40 mg. and 80 mg. in order to achieve film thicknesses between 1500 A^o and 3700 A^o . These tellurium films on Zn foil substrates or, in short, Zn/Te samples were used for Ion Beam Mixing experiments.

2.2. SURFACE MODIFICATIONS BY KRYPTON ION BOMBARDMENT

The Zn/Te samples were bombarded with 1 MeV Kr^{++} heavy ions at the Central Nuclear Facility, I.I.T. Kanpur. The bombardment fluences (doses) ranged from $6.7 \times 10^{+15}$ to $4.8 \times 10^{+16}$ Kr^{++} ions/cm^2 . The Central Nuclear facility houses the 2 MeV Van de Graaff Accelerator which provided the necessary ion

beams for this work. Appendix-A attempts to describe this facility in sufficient detail.

Kr^{++} beams have been standardised in this laboratory for study of heavy ion induced surface modifications. Due to limited capacity of the analyzing magnet (Appendix-A) at the accelerator facility, singly ionized Kr^+ ion beam cannot be steered into the 20° port (Figure A1,Appendix-A). Therefore doubly ionized Kr^{++} beams were used in this work. For doubly ionized Kr^{++} beam, the magnet current required for steering the beam into the 20° port, goes down by half. This reduced current is of about 175 amperes, which is well within the capacity of the magnet. The accelerator accelerates singly ionized Kr^+ ions. In the beam tube, just before the magnet , the vacuum is deliberately deteriorated to 7×10^{-5} torr to facilitate generation of double ionized Kr^{++} from singly ionized Kr^+ beam by charge exchange mechanism with the residual gas molecules in the beam pipe.

The variation of the Kr^{++} beam current (measured on the sample) with the pressure in the beam tube just before the magnet, for this accelerator facility was investigated by A.Tripathi [53] and is shown in Figure 2.2. A relation (Equation 2.2) between the number of doubly ionized projectiles (N^{++}) and the number of singly ionized ones (N^+) has been put forth by Picraux et al [33].

$$\frac{N^{++}}{N^+} = 6.5 \times P \text{ (torr)} \times l \text{ (cm)}$$

(2.2).

Here l is the length of the beam path. l and N^+ are fixed for this laboratory. N^+ depends on the characteristics of the ion

source of the Van de Graaff accelerator. Thus Equation 2.2 leads to a relation between N^{++} at two different pressures, which can be written as

$$\frac{N^{++} \ (\ Pressure \ P_1 \ )}{N^{++} \ (\ Pressure \ P_2 \ )} = \frac{P_1}{P_2}$$

(2.3).

For values of P_1 and P_2 equal to 7×10^{-5} torr and 1.5×10^{-5} torr the ratio of the respective N^{++} values at these two pressures turns out to be 4.6. From Figure 2.2 the Kr^{++} beam current for a pressure of 1.5×10^{-5} torr is 0.08 μA. Knowing this value the beam current at 7×10^{-5} torr pressure turns out to be 0.368 μA using the ratio 4.6 from Equation 2.3. The experimentally observed value from Figure 2.2 is 0.3 μA at 7×10^{-5} torr pressure . Thus this experimental fact agrees quite well with the above equation. Figure 2.3 shows the magnet currents required for steering various ion beams into the 20° port.

2.2.1   THE HEAVY ION IRRADIATION CHAMBER

Ion bombardments on Zn—Te samples were carried out in the heavy ion irradiation chamber shown in Figure 2.4. Prior to this work the same chamber was mounted on the usual oil diffusion vacuum system. Such a vacuum system is notorious for its residual hydrocarbon impurities. Figure 2.5 shows the RBS spectra taken for a pure Si wafers bombarded with 1 MeV Kr^{++} ions in this chamber mounted on a diffusion pump. The pronounced carbon peak is an indication of the hydrocarbon impurities left behind. Figure 2.5 shows an enhancement of the carbon peak under increased fluence of Kr^{++} irradiation.

It therefore became necessary to develop clean vacuum conditions under which Ion Beam Mixing experiments could be carried out. For this purpose a BALZERS turbomolecular pump. was installed just below the heavy ion irradiation chamber. The unique positioning of the turbomolecular pump is crucial in achieving higher pumpings speeds. All ion bombardment work presented in this thesis work was carried out in clean turbomolecular vacuum. It is noteworthy, that in all RBS results of Ion Beam Mixing in Zn-Te, carbon contamination is conspicuous by its absence.

In the center of the chamber is a movable ladder on which a number of samples can be mounted and by moving the ladder upwards or downwards by a predetermined amount the required sample can be introduced in the path of the Kr^{++} ion beam. The ladder is electrically isolated from the rest of the chamber by a perspex flange. A current integrator is connected to this ladder. It is capable of recording the total charge implanted on the sample by ion bombardment.

Surrounding the sample ladder is a cylinder made of aluminium sheet which has an opening for the passage of the heavy ion beam. This cylinder is maintained at a potential of nearly -260 volt relative to the grounded chamber. This arrangement is called a supressor which inhibits the emission of secondary electrons from the sample during Kr^{++} ion implantation. In the absence of such a supressor the secondary electron emission plays havoc with the measurement of total charge implanted in the sample during the heavy ion irradiation.

The beam which enters the chamber is collimated by the stabilizing slits (Figure A1,Appendix-A). By the time it reaches the chamber it spreads slightly and is further collimated by an aperture, mounted just before the sample ladder, of dimensions 9.0mm (vertical) x 3.0mm (horizontal). Thus an area of approximately these dimensions on the sample gets irradiated by the Kr^{++} ion beam.

Since the beam current/flux is more or less fixed the dose of Kr^{++} ions is adjusted by fixing the irradiation time. In order to estimate the beam uniformity, Kr^{++} irradiations were carried out on aluminium foils and the irradiated region was analysed by RBS. The doses of Kr^{++} irradiation at various points on the irradiated region were determined by using the following relation [56,57].

$$(N \cdot t) = \frac{A_{Kr}}{H_{Al}} \cdot \frac{\sigma_{Al}}{\sigma_{Kr}} \cdot \frac{\delta E}{[\epsilon]^{Al}_{Al}}$$

(2.4).

where Nt is the dose A_{Kr} represents the total integrated counts for the Kr peak in the backscattering spectrum for this Al foil, H_{Al} the height of the aluminium substrate height, σ is the cross section δE is the energy interval corresponding to each channel in the multichannel analyser. Figure 2.6 shows the variation of the Kr^{++} dose along the vertical direction. The Kr^{++} irradiation dose seems to be fairly uniform over the central region.

Another important point needs to be added as regards the sample temperature rise during heavy ion bombardment. If the temperature rise is too high then the

mixing due to thermal effects may become large enough. However at the ion currents current densities employed in this work viz 0.1 to 0.2 $\mu A/cm^2$ the expected sample temperature is about 20° to 30° K [54].

2.3. ION BEAM ANALYSIS (RUTHERFORD BACKSCATTERING)

Figure 2.7 gives the details of the RBS chamber. This chamber is mounted on a diffusion pump vacuum system with a liquid nitrogen trap which yields a vacuum of the order of 5.0×10^{-6} Torr. This vacuum is quite adequate for the RBS work.

Inside the chamber the samples are mounted on a ladder (electrically isolated from the grounded chamber) which is simillar to the one employed in the heavy ion irradiation chamber. A suppressor arrangement like the one used during the heavy ion irradiations is mounted in the chamber. The same current and charge measuring electronics used in the case of heavy ions is connected on the RBS chamber during ion beam analysis. On the side facing the beam, a quartz plate is fixed. The quartz plate gives out a blue glow when the $^4He^+$ beam falls on it. The purpose of this arrangement is to aid the allignment of the alpha beam.

Before entering the chamber the $^4He^+$ beam is collimated by X and Y slits to obtain a beam spot of about 1.0mm x 1.0mm dimensions or less.

The detector is mounted at a scattering angle of 150° and subtends a solid angle of about 2.0 millisteradians at the center of the beam spot. This silicon surface barrier detector sits on a cylinder through which flows chilled water.

The chilling helps in reducing the leakage currents in the surface barrier detector from 200 nA to 50 nA.

The electrical signals from the surface barrier detector were analysed by the usual nuclear electronics and multichannel analyser. Specifically, in these measurements an EG & G ORTEC 142A preamplifier, 572 amplifier 444 biased amplifier and ACE4096 Multichannel Analyser PC cards were used.

2.4. SCANNING ELECTRON MICROSCOPY (SEM) ANALYSIS

Figure 2.8(a) shows the SEM picture for a sample comprising of a glass substrate on which zinc and tellurium films were successively evaporated giving a zinc-tellurium bilayer structure of the type GLASS/Zn/Te. This picture was taken at 2000 magnification on the borderline of the irradiated and unirradiated regions of the sample. The region studded with globules is the irradiated region. These gobules were verified to be tellurium globules by EDX analysis of the samples. It appears that the film segregates into tellurium globules under ion bombardment. Such "artifacts" can lead to very confusing and misleading RBS results.

For the samples studied in this thesis work such a globular formation is absent as can be seen in Figure 2.8(c). Figure 2.8(b) is the corresponding SEM picture for the Te surface of the as evaporated Zn/Te sample. This SEM analysis therefore conclusively eliminates confusion arising from surface artifacts.

One of the common features of ion bombardment at low doses is the increase in grain sizes in the samples. This

can be seen on comparison of Figures 2.8(b) and 2.8(c).

2.5. THE "TRIM" COMPUTATIONS

The "TRIM" program (1988 version) was used to estimate the range of Kr^{++} ions, displacements of target atoms, the straggling (statistical fluctuations) in the ion energies and the energy transferred to the recoiling zinc and tellurium atoms in the Zn/Te samples.

The program takes, as input, the incident ion energy, the tellurium and zinc thicknesses, the displacement energy E_d and the binding energy of the lattice atom to its site E_b .

This software assumes an incident ion of atomic number Z_1 and energy E_1. It undergoes a collision with a target atom of atomic number Z_2, which acquires energy E_2 following collision. For such a model the following possibilities exist :

CONDITION	CONSEQUENCE
1 $E_1 > E_d$, $E_2 > E_d$	A vacancy results.
2 $E_1 > E_d$, $E_2 < E_d$	E_2 is released in the form of phonons.
3 $E_1 < E_d$, $E_2 > E_d$	Original atom remains at the site. The event is then called a "Replacement Collision."
4 $Z_1 \neq Z_2$	Z_1 becomes an antisite lattice atom.
5 $Z_1 = Z_2$	Z_2 merely replaces Z_1 in the cascade and E_1 is released in the form of phonons.
6 $E_1 < E_d$, $E_2 < E_d$	Z_1 becomes an interstitial and $E_1 + E_2$ is released in the form of phonons.

The "TRIM" calculations were performed for two

cases. One with tellurium thickness equal to 3400 Å and the other with the same equal to 2000 Å. The zinc thicknesses were arbitrarily given, taking care that the combined thickness of the zinc-tellurium structure was much beyond the range of the krypton ions. This was confirmed by the absence of transmitted ions in the "TRIM" outputs. The calculations were performed for successive bombardment with more than 2000 ions to get a good statistical picture.

CHAPTER 3

ANALYSIS, RESULTS AND DISCUSSION

All RBS spectra (taken in the case of two tellurium thickness categories centering around 2000 $\overset{o}{A}$ and 3400 $\overset{o}{A}$ respectively) , were analysed using the widely used, DOS based "RUMP" package. Simulations were performed, using this programme, for each RBS spectrum to get a better understanding of the ion induced atomic mixing process in the Zn/Te samples. Concentration profiles, fed in the program for simulating the RBS spectra, were used for calculating the amount of mixing.

3.1 CALCULATION OF DOSE / FLUENCE OF ION IRRADIATION

The aluminium samples ,bombarded with Kr^{++} ions under the same conditions as those for Kr^{++} irradiations on the Zn/Te samples, were used for estimating the dose of Kr^{++} ions (Appendix-B), However for maintaining accuracy of the dose calculation it was necessary to calculate the dose from the same Zn/Te sample from sputtering data.

It is a well known fact that the phenomenon of sputtering under ion irradiation varies linearly with the ion dose. Experimental and theoretical trends [49] indicate that the sputtering yield for elements with masses comparable to Te is approximately 10 for 1 MeV Kr^{++} ions. For example S for silver is 10, that for cd is 9, and for tungsten which is slightly heavier than Te the corresponding value is 20.

Therefore the S value was assumed to be 10 tellurium.

The dose of Kr^{++} ion irradiation was calulated using the following relation

$$\phi = \frac{\Delta \, X_S \cdot N_{Te}}{Y}$$

(3.1).

where $\phi = Kr^{++}$ ion dose,

$\Delta \, X_S$ = thickness of tellurium sputtered,

N_{Te} = bulk atomic density (number of atoms per unit volume) of tellurium,

and Y = the sputtering yield. This relation can be easily derived from the basic definition of sputtering yield. The ion dose was found to range from $6.67 \times 10^{+15}$ Kr^{++}/cm^2 to $4.77 \times 10^{+16}$ Kr^{++}/cm^2.

3.2. SIMULATIONS OF RUTHERFORD BACKSCATTERING SPECTRA

The simulations of RBS spectra, using "RUMP", need as input, the concentration profiles of Zn and Te, right upto about 20000 Å from the surface. A mental conception of the sample has to be fed into the programme. This conception was in the form of layers, numbering upto six, including the substrate. The total thickness of this multilayer structure was estimated by preliminary analysis of the RBS spectra (Appendix-B). For each layer a uniform matrix composition was specified. The specification for each layer also included a linear variation in the composition of any diffusant like zinc, tellurium or oxygen. To illustrate the structure fed, the input for simulation of the RBS spectrum of the thick sample for $4.298 \times 10^{16} Kr^{++}$ ions/cm^2 dose is shown is displayed in Table 3.1.

The computer generated output for this mental conception was superimposed with the actual RBS spectrum. Perfect matching of the simulated and the RBS spectrum requires careful adjustments of the thickness, the matrix composition, and the linear variation of the diffusant concentration for each of the sublayers of this imagined layered structure. When the simulation exactly matches the actual spectrum, one arrives at the correct zinc and tellurium concentration profiles for the actual sample. These concentration profiles were then used to calculate the Kr^{++} ion irradiation fluence/dose.

3.3. CALCULATION OF ATOMIC MIXING UNDER ION IRRADIATION

The zinc and tellurium concentration profiles fed in the "RUMP" program for simulatons were superimposed. The thickness of overlap region, taken as the one over which the concentration profiles continuously fall, without abrupt discontinuities, is shown in Figure 3.4(b). This thickness of the intermixed region is a measure of atomic mixing process in the Zn/Te system. All Figures of simulation profiles shown also display the concentration profiles of Zn and Te, which were fed in the "Rump" program to get good simulations.

3.4. THE "TRIM" RESULTS

Figures 3.16 to 3.25 show the results of the "TRIM" calculations for the two thickness cases. Figure 3.16 is a graphic display of the of the ion cascade for about 2700 krypton ions. Figure 3.17 shows the distribution of the ions throughout the Zn/Te model giving a mean range of 3436 Å . This was approximately the value chosen for the thicker tellurium

film samples.Figure 3.18 shows the depth distribution of displacement events. Figure 3.19 shows the lateral straggling in the ions resulting in a mean straggling of about 1092.11 $\overset{o}{A}$, which is negligibly small compared with the dimensions of the ion bombarded region in the Zn/Te samples (approximately 3 mm x 9 mm). Lateral straggling becomes relevant only when the ion irradiated regions are of very small dimensions as in the case of VLSI circuits. Figure 3.20 shows the profile for the transfer of ion energies to the lattice atoms. Comparing Figure 3.18 with Figure 3.20, one can say that the simillarity between the two profiles is an indication of ion energy dissipation via displacement of target atoms. The maxima of the plot in Figure 3.18 (and also Figure 3.20) lies at about 2000 $\overset{o}{A}$ from the tellurium surface. This was therefore the value chosen for the tellurium films in the case of the thinner tellurium film samples. Figures 3.21 to 3.25 are simillar outputs for the thin tellurium thickness category.

3.5. DISCUSSION OF THE RESULTS

A > COMMENTS ON THE RBS RESULTS

For all as evaporated spectra (spectra taken at points, on the sample surface, shielded from Kr^{++} bombardment), good simulations were possible. The simulation inputs involved a 500 $\overset{o}{A}$ to 700 $\overset{o}{A}$ zinc oxide layer at the zinc-tellurium interface. This was to be expected because the zinc substrates were prepared in normal atmosphere. The surface of the zinc substrates gets quickly oxidized after etching. The tellurium films were deposited on these substrates thus leaving a zinc oxide layer at the interface. The presence of the zinc oxide

layer is shown in Figures 3.2 and 3.10. The interface oxygen seems to vanish under Kr^{++} irradiation. Further, in the case of those RBS spectra taken at high dose points (Figures 3.13 (a), 3.14 (a)), there appears to be surface oxygen. It is a possibility that the zinc emerging at the surface as a result of Kr^{++} irradiation gets oxidized, manifesting itself in the form of the slight hump at the oxygen surface energy position in the RBS spectra.

Figure 3.1 shows the RBS spectra for the thicker tellurium samples taken for various Kr^{++} doses. The gradual reduction in area under the tellurium peak with increasing doses is indicative of gradual increase in sputtering. The positions of the various elements marked, show the energies of the backscattered He^+ particles from these, had these elements been present on the surface. It can be seen that, with increasing doses, the zinc edge in the RBS spectra gradually approaches the zinc surface energy position marked. This means that zinc progressively moves closer to the surface with increasing Kr^{++} dose. Simillarly the tail of the tellurium peak moves deeper into the substrate.

The mixed amounts vary linearly with the square root of the dose as shown in Figure 3.15 .This is a distinct signature of atomic mixing through the mechanism of Radiation Enhanced Diffusion. Thus it appears that defect production and migration controll the mixing process [25]. A summary of quantitative low temperature (including room temperature) measurements on bilayer samples presented in a review article [8], shows that a majority (with very few exceptions) of bilayer systems exhibit this $\phi^{1/2}$ dependence. This appears to

be a characteristic feature of ion beam mixing at non-elevated sample temperatures during ion bombardment. The Zn/Te samples studied in this work also seem to conform to this general rule. For higher doses the mixed thickness falls sharply due to sputtering of the mixed thickness. It can be seen that the highest mixed thickness spectrum shows the presence of zinc on the surface of the sample. Thus, one can see that the mixed zone spreads from the interface towards the surface with increasing dose. Meanwhile, the sputtering process at the tellurium surface goes on incessantly. The thickness of the mixed zone increases untill the edge of this zone reaches the surface. At this stage the sputtering process commences the erosion of the mixed zone. Consequently, the thickness of the mixed zone, with further increase in dose, sharply falls.

The difference in slope of the mixing versus square root of dose $\phi^{1/2}$ plots for the two different tellurium film thicknesses is a manifestation of the difference in the Kr^{++} ion energies at the zinc-tellurium interfaces of the two categories of samples. For the smaller tellurium thickness case, the Kr^{++} ions travel through lesser distance in tellurium and consequently have higher energy at the interface. As a result greater mixing is observed as compared with the thicker tellurium film samples for the same dose. This was also expected on the basis of the "TRIM" calculations (Section 3.5 B).

B > DISCUSSION OF THE TRIM RESULTS

According to the "TRIM" calculations, the maximum dissipation of ion energy should occur at 2000 Å below the tellurium surface. The Zn/Te samples show greater mixing in the

case of the thinner tellurium film samples as compared with the thicker ones (for the same dose). Thus the experimental results appear to be consistent with the "TRIM" predictions.

C >   X-RAY DIFFRACTION STUDIES

Figure 3.26 shows the results of the X-ray diffraction analysis of the samples. Presence of small regions of zinc telluride cubic phase. has been observed in the post bombardment X-Ray diffraction plots. Two of the major peaks were observed indicating the formation of a thin layer of zinc telluride compound. Due to the presence of the zinc substrates, which is about 0.2 to 0.3 mm thick, the X-Rays scattered from the planes of this cubic phase are of extremely weak as compared to those arising from the substrate. This prevents the weaker ZnTe peaks from being identified. Further, in the case of thin films, certain peaks could get accentuated and others supressed due to alignment of the grains in certain preferred directions.

Concentration profiles for zinc and tellurium obtained from the RBS studies also indicate continuously varying zinc and tellurium concentrations. This leaves a small thickness over which the zinc and tellurium atoms are in equal numbers. It is over this small region that one expects a layer of zinc telluride compound. The 220 and 311 peaks appearing shown in Figure 3.26 support this contention.

CONCLUSIONS &

SUGGESTIONS FOR FUTURE WORK

CONCLUSIONS

Ion beam mixing in the zinc tellurium metal-metal system studied in this thesis work exhibits the square root dependence on dose. This points at the *Delayed Processes* viz. *Radiation Enhanced Diffusion* as the main mixing mechanism at work in the sample at ambient irradiation temperatures. The sample temperatures, during irradiations which took a maximum of one hour in the higher dose irradiations, are not expected to rise above 30° to 40° C. Thus one can say that the thermal diffusion effects for this temperature and irradiation times would be negligibly small. It therefore means that the radiation induced creation and migration of defects are responsible for the mixing process in addition to the ballistic mixing processes occuring in the first few picoseconds after ion-entry into the solid.

The existence of zinc telluride cubic phase, even though in small amounts, has been confirmed. This phase does not extend over a large thickness and is probably so because of excessive sputtering of Te atoms and of Zn atoms as and when they arrive at the surface.

Importance of clean vacuum conditions was felt throughout the period of this thesis work. The suitability of the clean vacuum set-up using the turbomolecular pump has been experimentally demonstrated.

SUGGESTIONS FOR FURTHER WORK

The problem of excessive sputtering can possibly be avoided by depositing a thin layer, of a material with a low sputtering coefficient like aluminium, of about a few hundred angstroms on the top of this bilayer. Such a cap will not inhibit the mixing process and at the same time prevent sputtering of the zinc and tellurium atoms. For 1 MeV kr beams, in the top few hundred angstroms the probability of collision would be very low. Hence one expects that the aluminium cap will not interfere in the ion beam mixing studies and also overcome the problem of sputtering.

During this thesis work there was an experimental difficulty in deposition of zinc films. The glass samples on which the SEM photographs showing the globular formations were taken showed poor reproducibility of zinc film depositions. It is difficult to achieve condensation of zinc on the surface. Substrates have to be cooled to aid this condensation. Such a substrate cooling arrangement was designed in this laboratory by S.Singh [55]. It would now be possible to evaporate zinc films on various substrates. By successively evaporating zinc and tellurium one after the other without breaking the vacuum, it would be possible to avoid the zinc oxide layer at the zinc-tellurium interface. Deposition of zinc and tellurium on inert substrates like amorphous SiO_2 and then studying ion beam mixing in such a bilayer would be interesting for a number of reasons. Firstly the RBS spectra of such samples would be "clean." The substrate comprising of only light elements like silicon or oxygen would be well seperated from the zinc and

tellurium in the RBS spectra. Secondly, with either this configuration or with a multilayer configuration the limited zinc and tellurium condition can be created. The X-ray diffraction studies on this type of amorphous substrate would be quite revealing, since the amorphous substrate will not introduce its own peaks in the X-Ray diffraction plots. Fourtly, a such a non conducting substrate opens up the possibility of electrical characterization of the irradiated films.

In this laboratory an attempt is being made to increase the uniformity of the Kr^{++} irradiation dose over the entire bombarded region. For this purpose a beam profile monitor was installed on the heavy ion port. This monitor will make it possible to select the most uniform portion of the beam. Such uniform beam spots will help in reducing the error in dose measurements thus making the ion beam mixing study more accurate. Coupled with an arrangement to oscillate or vibrate the sample during irradiation, this set-up could manage to obtain a larger region of uniform dose bombardment. This would aid in the electrical measurements of the modified regions as mentioned above, as four probe contacts can be easily fixed over a larger irradiated zone.

It is further suggested that a liquid nitrogen cooled cylinder be fabricated so as to surround the sample holder inside the chamber during bombardment. This would result in better clean vacuum conditions and in supression of hydrocarbons during irradiation.

R E F E R E N C E S

1). P.D.Townsend, Contem. Phys., 27(3), 241-256 (1986).

2). J.M.Poate, G.Foti, D.C.Jacobson,"Surface Modification and Alloying by Laser, Ion and Electron Beams," (Plenum, New York 1983).

3). T.E.Seidel,"V.1.S.I. Technology" edited by S.M.Sze (McGraw Hill, New York 1983).

4). Peter H.Rose, Nucl. Instrum. Meth. Phys. Res., B35, 535-540 (1988).

5). J.F.Ziegler, Nucl. Instrum. Meth. Phys. Res., B6, 270-282 (1985).

6). Z.L.Liau, J.W.Mayer, J. Vac. Sci. Tech., 15(5) (1978).

7). J.K.Hirvonen, J.M.Poate, Z.L.Liau, J.W.Mayer (unpublished), see ref.6

8). B.M.Paine, R.S.Averback, Nucl. Instrum. Meth. Phys. Res., B7/8, 666-675 (1985).

9). U.Littmark, W.O.Hofer, Nucl. Instrum. Meth. Phys. Res., 168, 329-342 (1980).

10). P.Sigmund, A.Gras-Marti, Nucl. Instrum. Meth. Phys. Res., 182/183, 25-41 (1981).

11). G.H.Vineyard, Radiation Effects, 29, 245-248 (1976).

12). J.A.Brinkman, J. Appl. Phys. 25, 961 (1954).

13). G.J.Clark, A.D.Marwick, D.B.Poker, Nucl. Instrum. Meth. Phys. Res., 209/210, 107 (1983).

14). J.Bottiger, S.K.Nielsen, P.T.Thorsen, Nucl. Instrum. Meth. Phys. Res., B7/8, 70 (1985).

15). R.Sizmann, J. Nucl. Mater., 69/70, 386 (1968).

16). G.J.Dienes, A.C.Damask, J. Appl. Phys., 29(12), 1713 (1958).

17). J.C.Bourgoin, J.W.Corbett, Radiation Effects, 36, 157-188 (1978).

18). S.Matteson, B.M.Paine, M.G.Grimaldi, G.Mezey, M-A.Nicolet, Nucl. Instrum. Meth. Phys. Res., 182/183, 43 (1981).

19). S.Matteson, G.Mezey, M-A.Nicolet,"Thin Film Interfaces and Interactions," edited by J.E.E.Baglin and J.M.Poate, (Electrochemical Society, New Jersey 1980).

20). B.M.Paine, M-A.Nicolet, R.G.Newcomb, D.A.Thompson, Nucl. Instrum. Meth. Phys. Res., 182/183, 115 (1981).

21). F.Besenbacher, J.Bottiger, S.K.Nielsen, H.J.Whitlow, Appl. Phys, A29, 141 (1982).

22). S.T.Picraux, D.M.Follstaedt, J.Delafond, "Metastable Materials Formation by Ion Implantation," edited by S.T.Picraux, W.J.Choyke, (Elsevier, North Holland, New York, 1982), P.71.

23). T.C.Banwell, B.X.Liu, I.Golechi, M-A.Nicolet, Nucl. Instrum. Meth. Phys. Res., 209/210, 125 (1983).

24). C.T.Chang, S.U.Campisano, S.Cannavo, E. Rimini, J. Appl. Phys., 55, 3322 (1984).

25). R.S.Averback, L.J.Thompson, J.Moyle, M.Schalit, J. Appl. Phys., 53, 1342 (1982).

26). B.Y.Tsaur, S.S.Lau, L.S.Hung, J.W.Mayer, Nucl. Instrum. Meth. Phys. Res.,182/183, 67 (1981).

27). J.W.Mayer, B.Y.Tsaur, L.S.Hung, Nucl. Instrum. Meth. Phys. Res., 182/183, 1 (1981).

28). A.A.Galuska, Nucl. Instrum. Meth. Phys. Res., B47, 7-14 (1990).

29). K.Hohmuth, B.Rauschenbach, Nucl. Instrum. Meth. Phys. Res., B46, 276-283 (1990).

30). B.X.Liu, W.L.Johnson, M-A.Nicolet, S.S.Lau, Appl. Phys. Lett., 42, 45 (1983).

31). J.A.Alonso, S.Simozar, Solid State Communications, 48(a), 765-67 (1983).

32). B.X.Liu, B.M.Clemens, R.Gaboriaud, W.L.Johnson, M-A.Nicolet, Appl. Phys. Lett. 42(7), 624 (1983).

33). S.T.Picraux, Thin Solid Films, 19, 371, (1973).

34). B.Y.Tsaur, S.Matteson, G.Chapman, Z.L.Liau, M-A.Nicolet, Appl. Phys. Lett., 35, 825 (1979).

35). S.Matteson, B.M.Paine, M-A.Nicolet, Nucl. Instrum. Meth. Phys. Res., 182/183, 53 (1981).

36). S.Matteson, J.Roth, M-A.Nicolet, Radiation Effects, 42, 217 (1979).

37). B.X.Liu, Phys. Stat. Solid (a), 94, 11 (1986).

B7/8, 657 (1985).

39). S.T.Johnson, C.Cozzolino, J.S.Williams, Nucl. Instrum. Meth. Phys. Res., B19/20, 762-766 (1987).

40). C.J.Palmstron, K.L.Kavanagh, M.J.Hollis, S.D.Mukherjee, J.W.Mayer, Mater. Res. Sympo. Proc., 37, 473 (1985).

41). T.kazvo, F.Seijiro, J. Appl. Phys., 56(2), 560 (1984).

42). S.R.Smith, J.S.Solomon, Mater. Lett., 3(7,8) (1985).

43). C.W.White, G.Farlow, J.Narayan, G.J.Clark, J.E.E.Baglin, Mater. Lett., 2, 367 (1984).

44). J.E.E.Baglin, A.G.Schrott, R.D.Thompson, K.N.Tu, A.Segmüller, Nucl. Instrum. Meth. Phys. Res., B19/20, 782 (1987).

45). T.Banwell, B.X.Liu, I.Golecki, M-A.Nicolet, Nucl. Instrum. Meth. Phys. Res., 209/210, 125 (1983).

46). T.Banwell, M-A.Nicolet, T.Sands, P.J.Grunthaner, Appl. Phys. Lett., 50, 591 (1987).

47). G.Battaglin, S.Lo.Russo, A.Paccagnella, G.Principi, P.Q.Zhang, Nucl. Instrum. Meth. Phys. Res., B27, 402 (1987).

48). P.Q.Zhang, G.Principi, A.Paccagnella, S.Lo.Russo, G.Battaglin, Nucl. Instrum. Meth. Phys. Res., B28, 561 (1987).

49). H.H.Andersen, H.L.Bay, R.Behrisch, M.T.Robinson, H.E.Roosendaal, P.Sigmund, "Sputtering by Particle Bombardment-I," edited by R.Behrisch (Springer Verlag Berlin 1981).

50). G.Battaglin, S.Lo.Russo, A.Paccagnella, P.Polato, G.Principi, Nucl. Instrum. Meth. Phys. Res., B39, 126 (1989).

51). Bulent M.Basol, Vijay A.Kapur, Thin Solid Films, 165, 237-241 (1988).

52). J.Kimmerle, R.Menner, H.W.Schock, A.Valera, Thin Solid Films, 126, 23 (1985).

53). A.Tripathi, "Fabrication of an Irradiation Chamber and Study of Ion Beam Mixing of gold in Metglass $Fe_{79}B_{16}Si_5$ using MeV Kr Ion Beam," M.Sc. Thesis, Department Of Physics, Indian Institute Of Technology Kanpur (1990).

54). G.Dearnaley, J.H.Freeman, R.S.Nelson, J.Stephen, "Defects in Crystalline Solids : Ion Implantation," Vol.8, edited

by S.Amelinckx, R.Gevers, J.Nihoul (Elsevier, North
Holland 1973).pp 421-427.

55). S.Singh, M.Sc. Thesis, Department of Physics, Indian
Institute Of Technology Kanpur (1991).

56). "Backscattering Spectrometry," W.Chu, J.W.Mayer,
M-A.Nicolet, Academic Press (1978).

57). "Ion Beam Handbook For Material Analysis," edited by
J.W.Mayer, E.Rimini, Academic Press (1977).

.

*

.
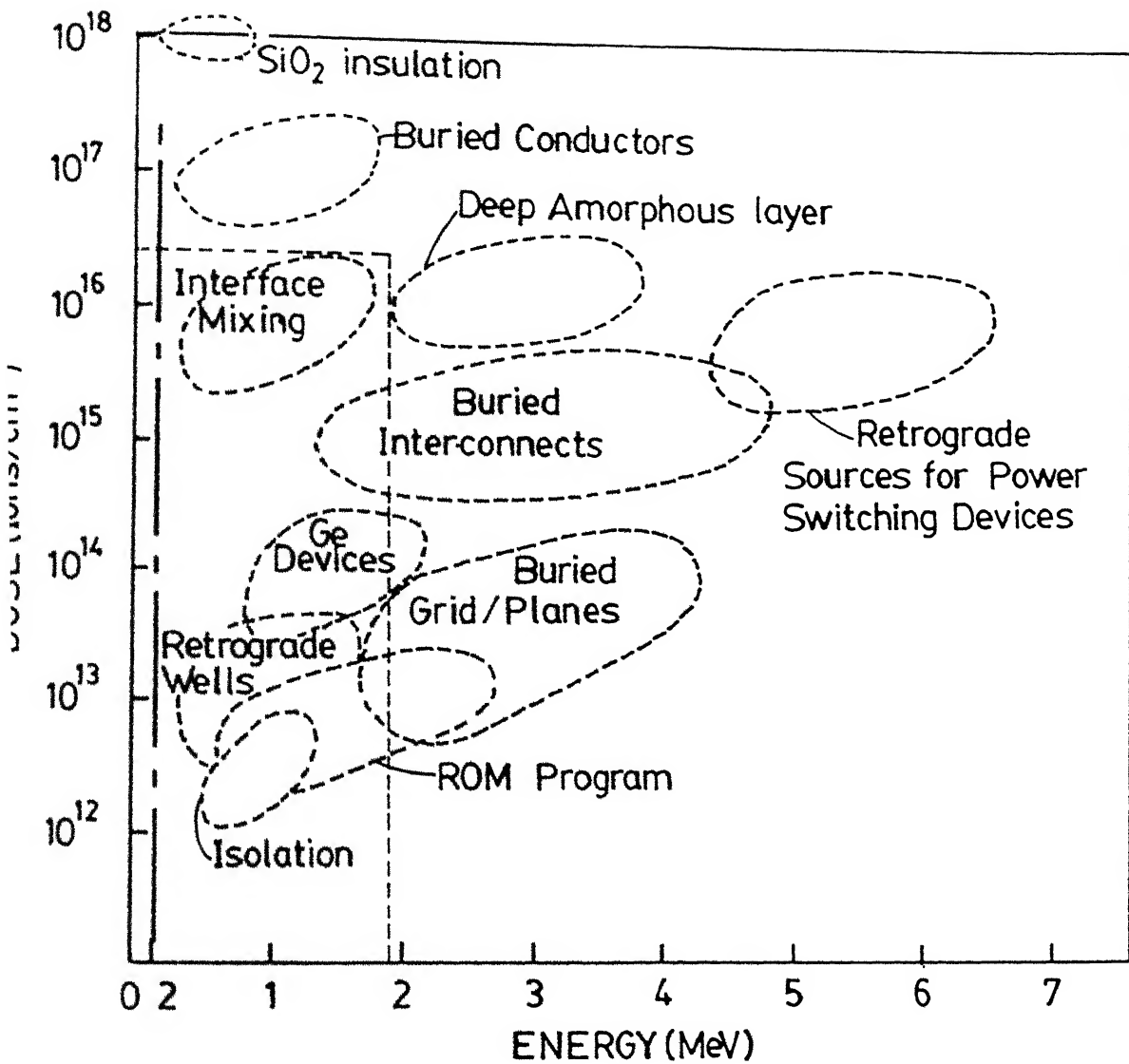
DOSE AND ENERGY RANGES FOR TYPICAL
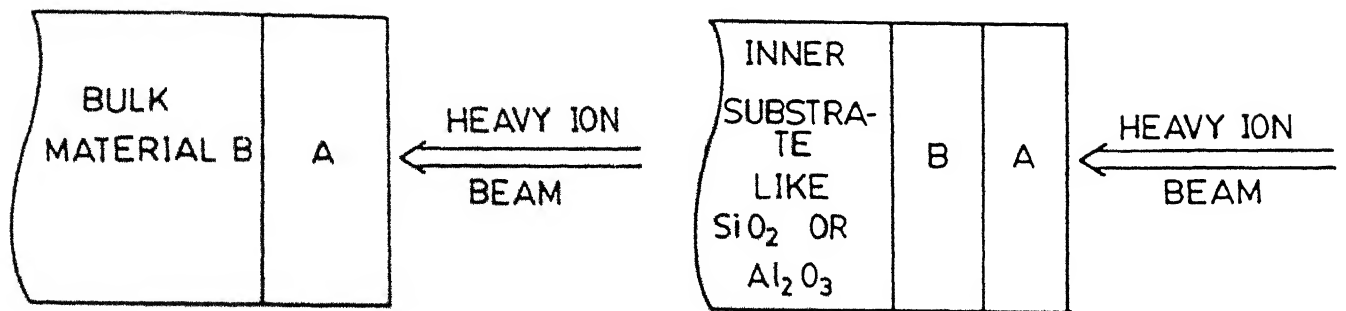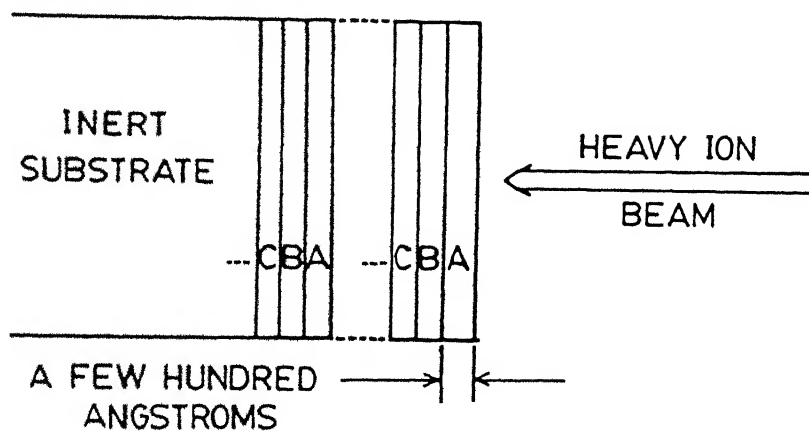APPLICATION OF HIGH ENERGY IMPLANTATION.

FIG. 1.1

Legend:
- ○ NORMAL ATOM
- ● INTERSTITIAL ATOM
- —— PATH OF PRIMARY PARTICLE
- ---- PATH OF PRIMARY KNOCK-ON

FIG. 1.2

MARKER A

BULK
MATERIAL B

B

HEAVY ION
BEAM

~ 10 Å

A FEW HUNDRED
ANGSTROMS

(a) MARKER CONFIGURATION

BULK
MATERIAL B

A

HEAVY ION
BEAM

INNER
SUBSTRA-
TE
LIKE
SiO_2 OR
Al_2O_3

B | A

HEAVY ION
BEAM

(b) BILAYER CONFIGURATION

INERT
SUBSTRATE

HEAVY ION
BEAM

---CBA ---CBA

A FEW HUNDRED
ANGSTROMS

(c) MULTILAYER CONFIGURATION

FIG. 1.3

SUBSTRATE HOLDER

TANTALUM BOAT

BASE PLATE

AIR ADMITTANCE VALVE

LIQUID NITROGEN TRAP

BAFFLE VALVE

GAS INLET

WATER CIRCULATION TUBES

SILICONE OIL

DIFFUSION PUMP HEATER

DIFFUSION PUMP

GLASS DOME

RUBBER GASKET

ROUGHING VALVE

BACKING VALVE

AIR ADMITTANCE VALVE

THERMOCOUPLE GAUGE-HEAD

ROTARY PUMP

THERMAL-EVAPORATION SET-UP

FIG. 2.1

Kr++ BEAM CURRENT ON TARGET vs. PRESSURE IN THE BEAM PIPE (before magnetic analysis)
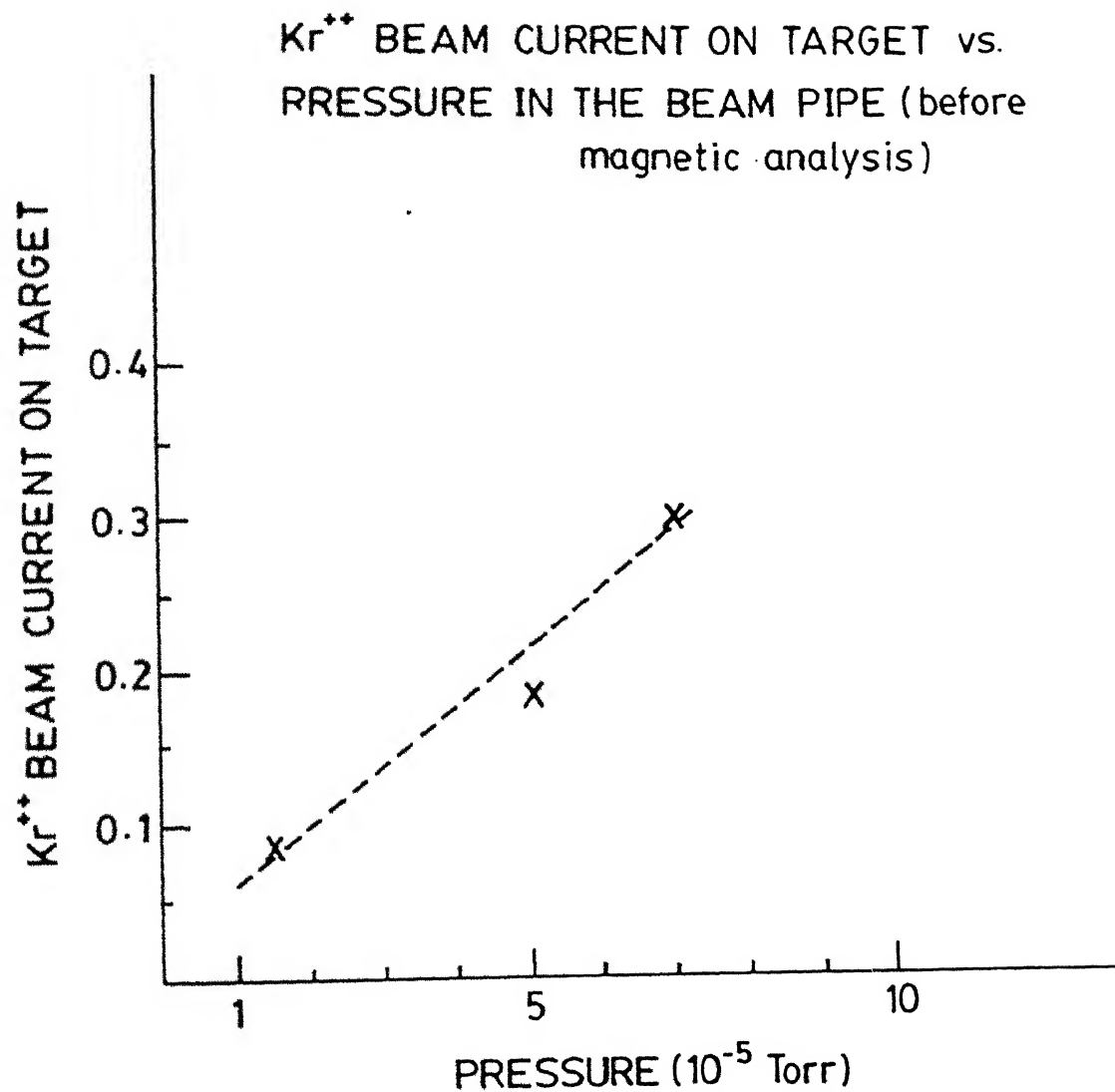
FIG. 2.2

HEAVY IONS

MAGNETICALLY ANALYZED BEAMS

DOME VOLTAGE : 1 MV
BEAM PORT : 20°
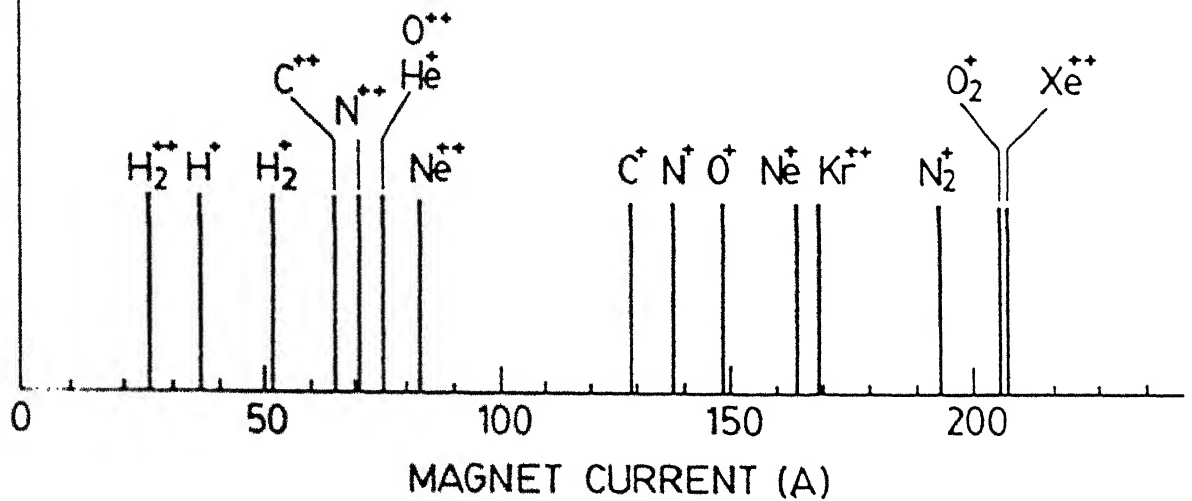
Note : The singly charged & doubly charged particles have same energy.

: Ionization occurs by stripping in the beam pipe after au^n & before magnetic analysis.

FIG. 2.3

MOVEABLE SHAFT

PERSPEX
INSULATING
FLANGE

SUPRESSOR.

MOVEABLE SAMPLE
HOLDER/LADDER

1 MeV Kr BEAM

QUARTZ
WINDOW

APERTURE

3mm × 9mm BEAM
SPOT

SAMPLE UNDER
IRRADIATION

TO PREVENT ANY
OBJECT FROM
FALLING ON THE
ROTATING TURBO
MOLECULAR
PUMP BLADES

FLAT
TABLE

WIRE
MESH

BELLOW

● - CROSS SECTION OF
O-RINGS

NOT DRAWN TO SCALE

TO TURBOMOLECULAR
PUMP
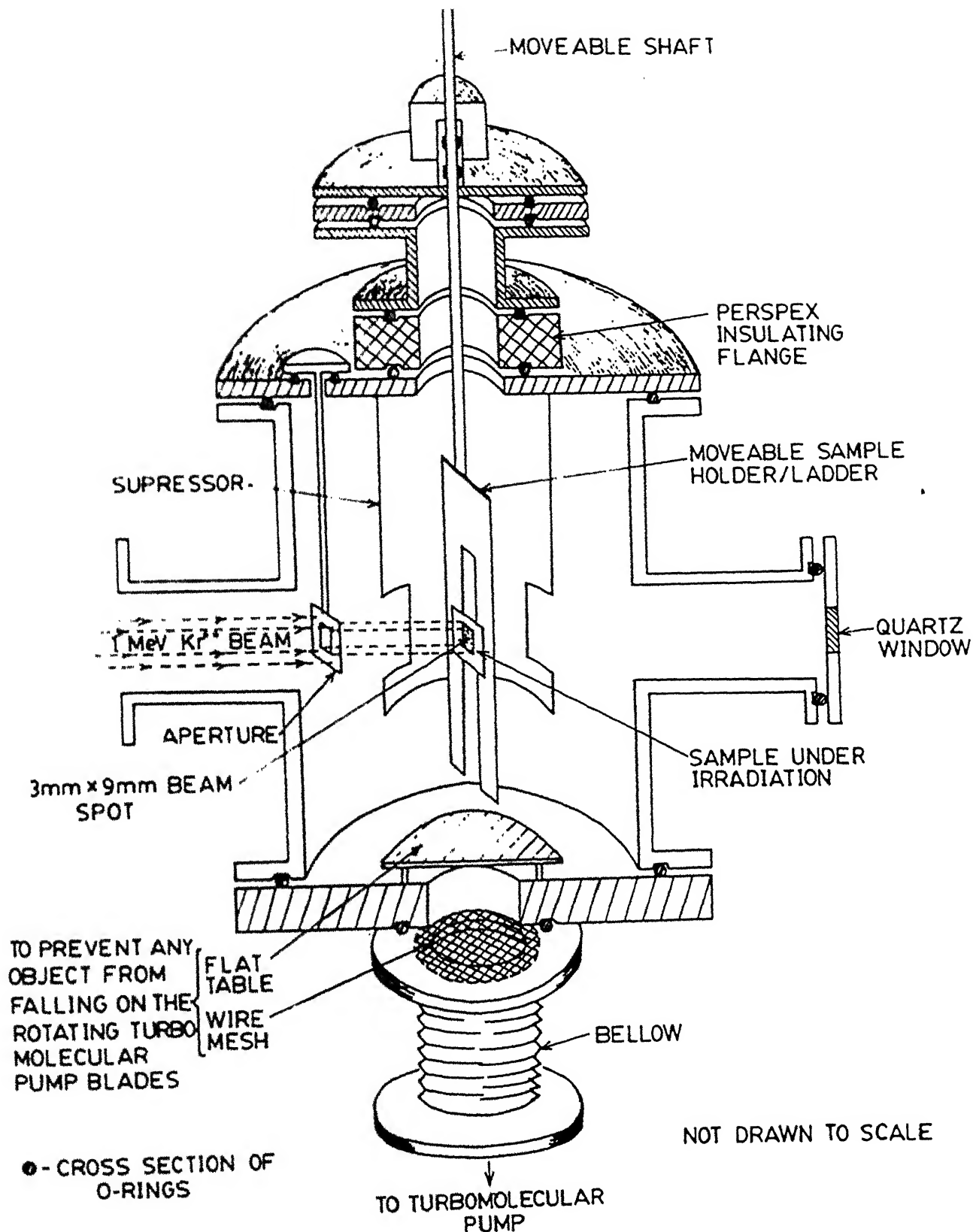
THE HEAVY
ION IRRADIATION CHAMBER

FIG. 2.4.
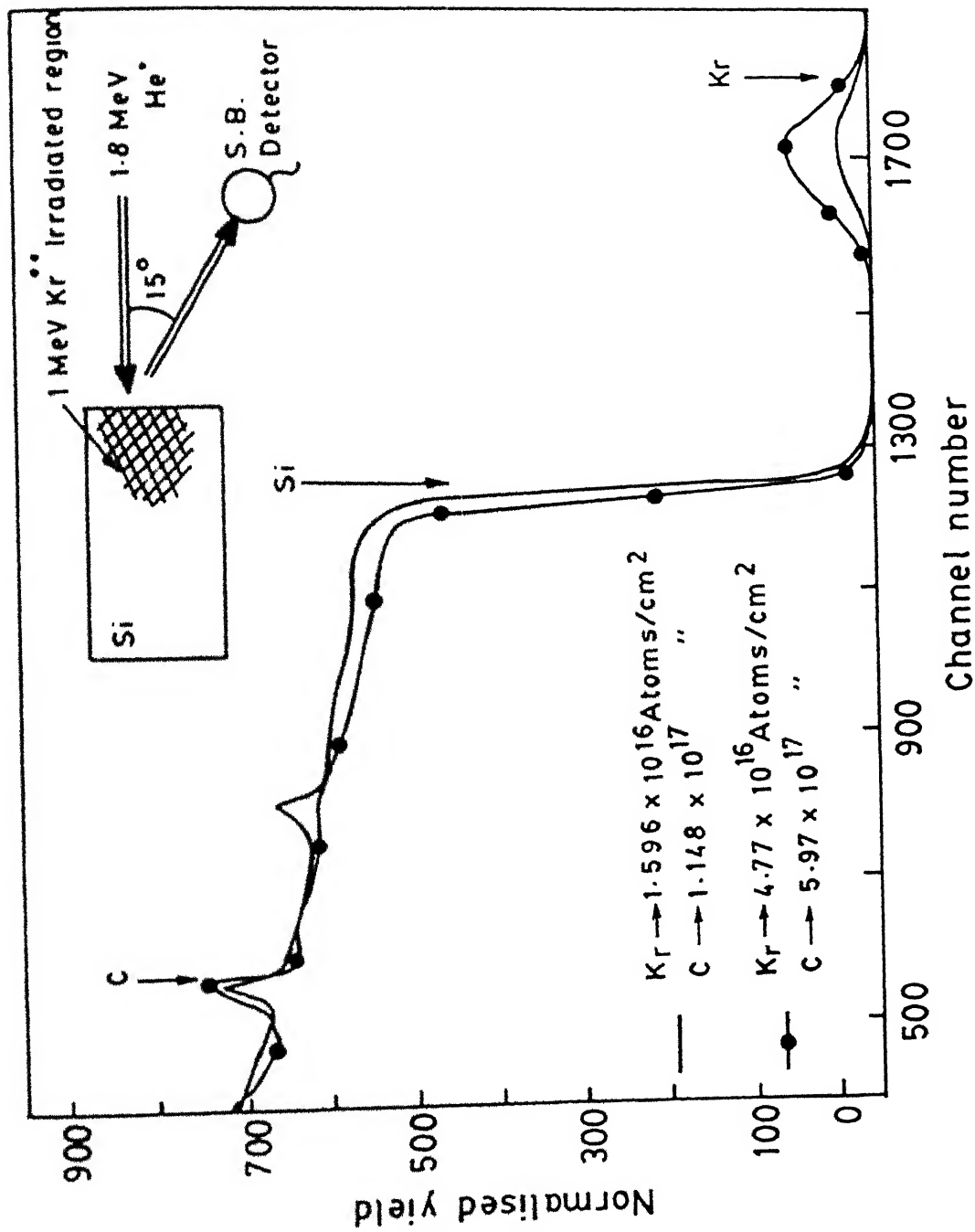
FIG. 2.5 APPEARENCE OF CARBON PEAK FOR Kr^{++} IRRADIATIONS IN OIL DIFFUSION PUMP VACUUM

VARIATION OF THE FLUENCE ACROSS THE BEAM
PROFILE IN THE VERTICAL DIRECTION

THE BEAM PROFILE

OBTAINED FROM RBS ANALYSIS OF
ALUMINIUM FOIL BOMBARDED WITH
1 MeV Kr^{++} IRRADIATION

DOSE/FLUENCE (10^{14} cm^{-2})

DISTANCE (mm) ⟶

FIG. 2.6

CURRENT INTEGRATOR

SCALER

CONTROL UNIT

GAUGE HEAD

NEGATIVE POTENTIAL FOR SUPPRESOR GRID

H.V.

MOVEABLE TARGET HOLDER

QUARTZ PLATE

INSULATING FLANGE

SUPPRESSOR GRID

S.B. DETECTOR

PREAMP--LIFIER

PULSER

AMPLIFIER

BIASED AMPLIFIER

MCA

OUT

FIG. 2.7

Fig 2.8(a)

Fig 2.8(b)

Fig 2.8(c)

FIG. 2.1

Figure content includes:

Axes: Normalized yield (vertical, from 50 to 200) vs Channel (horizontal, 0 to 500, with top scale 0.4 to 1.6)

Legend:
φ = Bombardment dose / fluence
φ = 0.667 × 10^{16} Kr^{++}/cm^2
φ = 3.360 × 10^{16} Kr^{++}/cm^2
φ = 4.081 × 10^{16} Kr^{++}/cm^2
φ = 4.298 × 10^{16} Kr^{++}/cm^2
φ = 4.769 × 10^{16} Kr^{++}/cm^2

— Te thickness prior to bombardment ≅3210.4 Å

Labels: Zn Kr Te, O, C

Diagram: 1.8 MeV He^+ , 30°, S.B. Detector, Zn | Te

FIG 2.2

(inputs for Simulation)

Atomic Fraction

Depth $\left(\begin{array}{c}\text{Thousands}\\\text{angstroms}\end{array}\right)$

□ Tellurium   △ Zinc

$$\phi = 0.664 \times 10^{16} \, Kr^{++}/Cm^2$$

FIG 3.3 (b)

FIG. 3.4 (a)

(Input for Simulation)

Atomic fraction

Depth (Thousands) (angstroms)

□ Tellurium   △ Zinc

$\phi = 1.652 \times 10^{16} \; Kr^{++}/cm^2$

FIG 3.4 (b)

FIG. 3.5 (a)

(Input for Simulation)
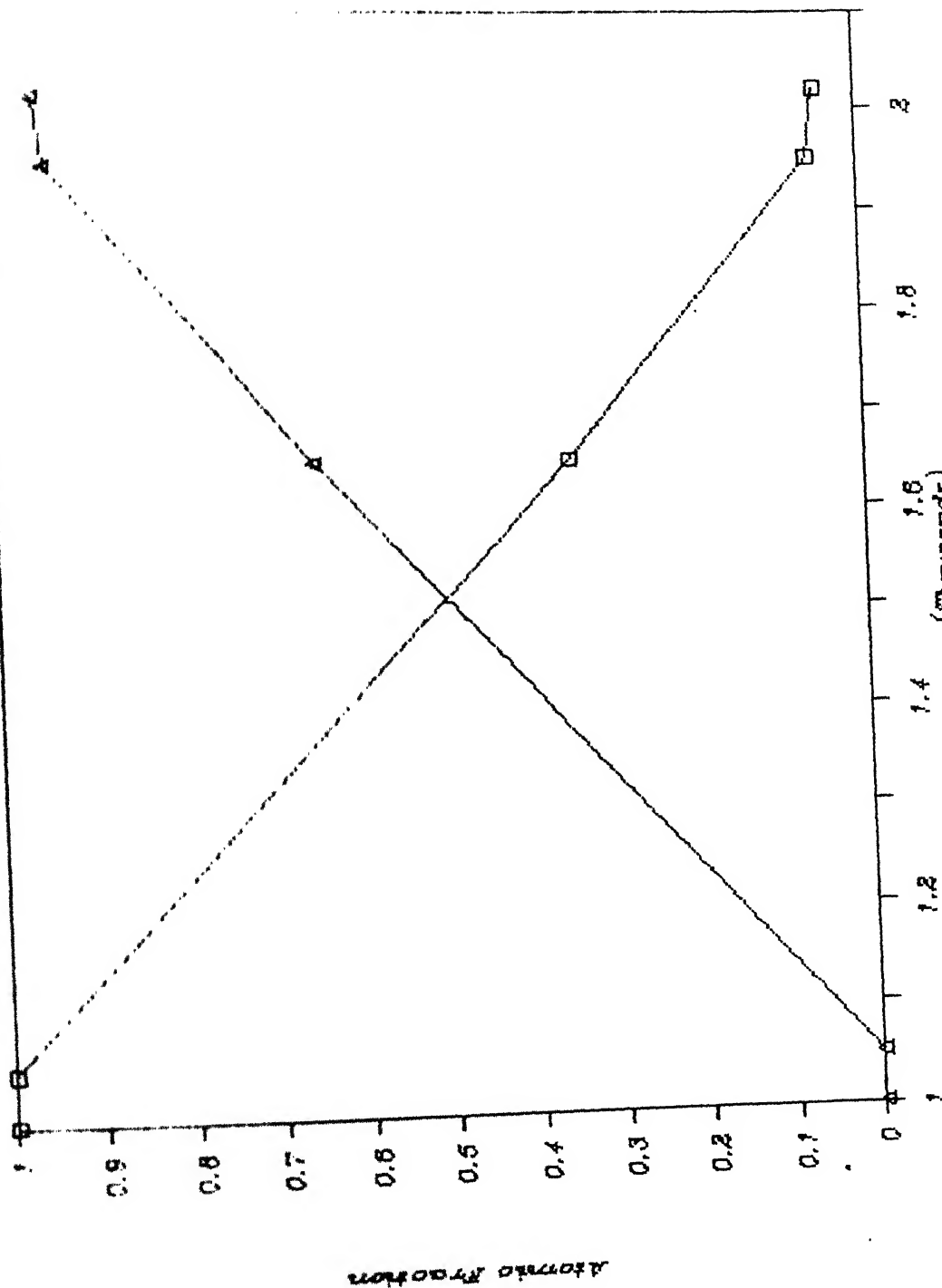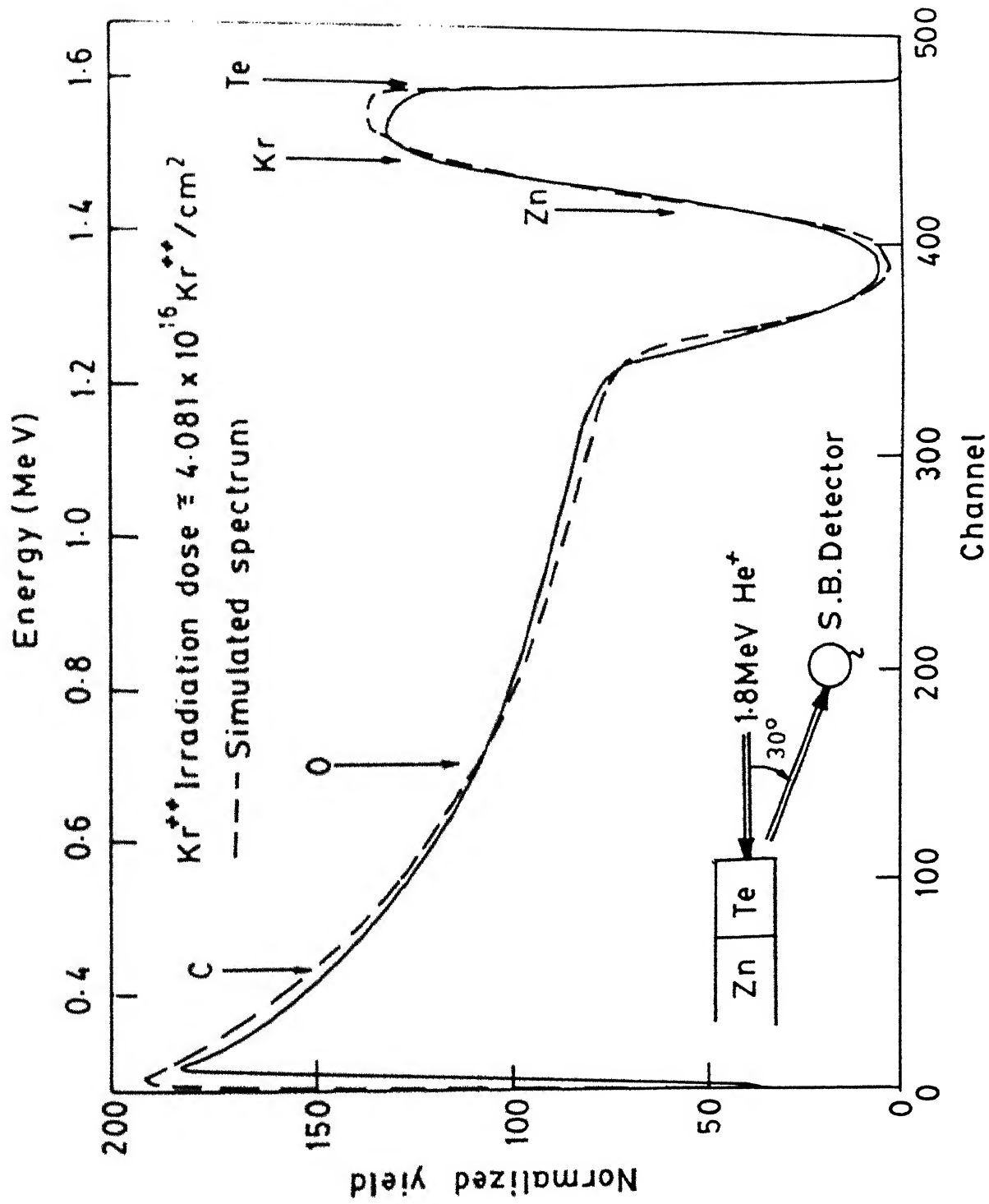
Atomic fraction

Depth (Thousands) (angstroms)

□ Tritiarium   △ Zinc

$\phi = 3.360 \times 10^{16} \, Kr^{++} / cm^2 \, (\lambda)$

FIG. 3.5

FIG. 3.6 (a)

(Input for Simulation)

Atomic Fraction

Depth $\left(\begin{array}{l}\text{Thousands} \\ \text{angstroms}\end{array}\right)$

□ Tellurium   △ Zinc

$\Phi = 4.081 \times 10^{16} \; Kr^{++}/cm^2$

FIG. 3.6 (b)

Energy (MeV)

Normalized yield

Kr^{++} Irradiation dose = 4.298×10^{16} Kr^{++}/cm^2
---- Simulated spectrum

1.8 MeV Kr^{++}
$30°$
S.B. Detector

Zn | Te

Channel

FIG. 3.7 (a)

Te & Zn Concentration Profiles

(input for Simulation)

Atomic Fraction

1
0.9
0.8
0.7
0.6
0.5
0.4
0.3
0.2
0.1
0

0.8   1   1.2   1.4   1.6
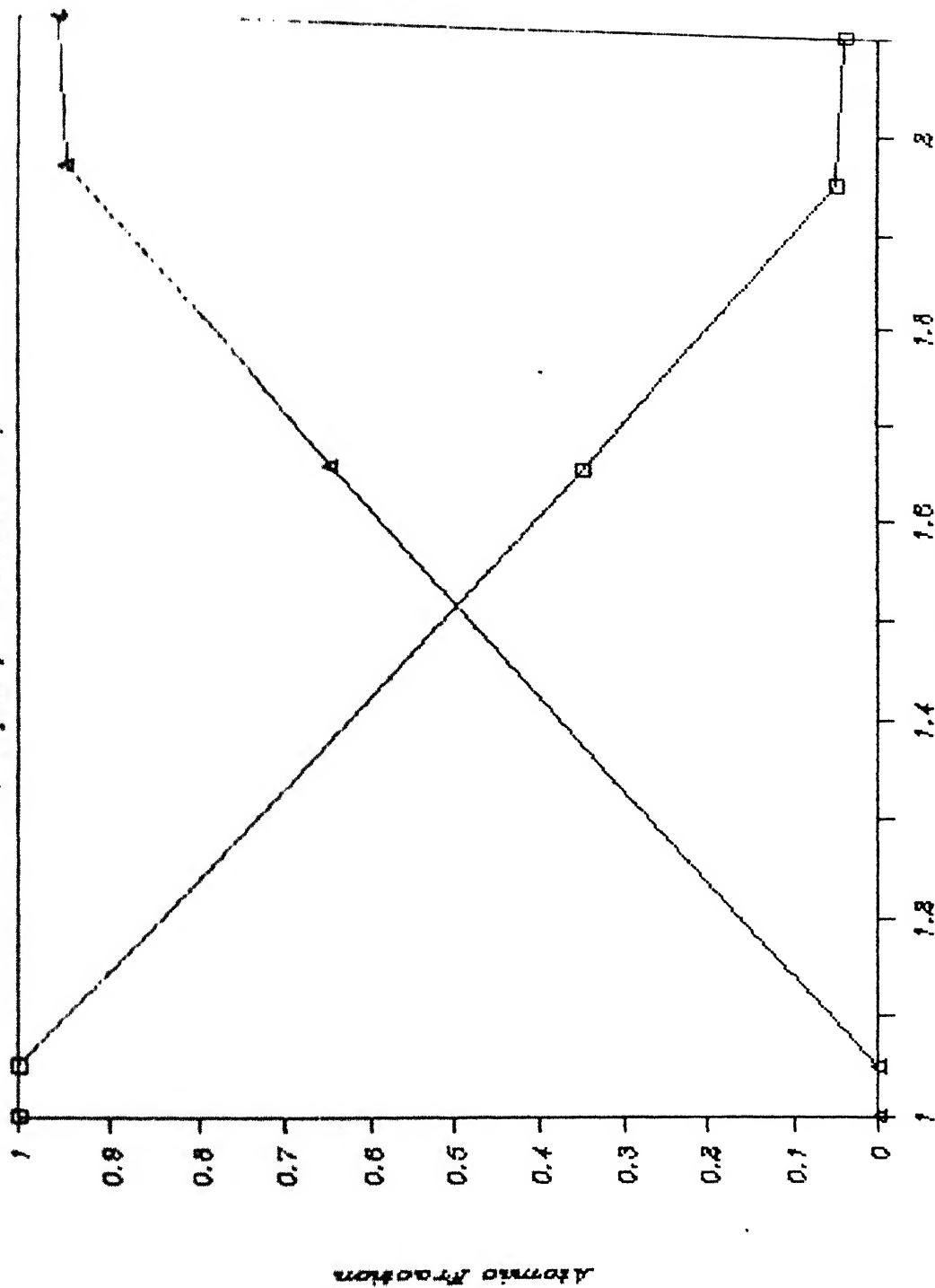
Depth (Thousands angstroms)
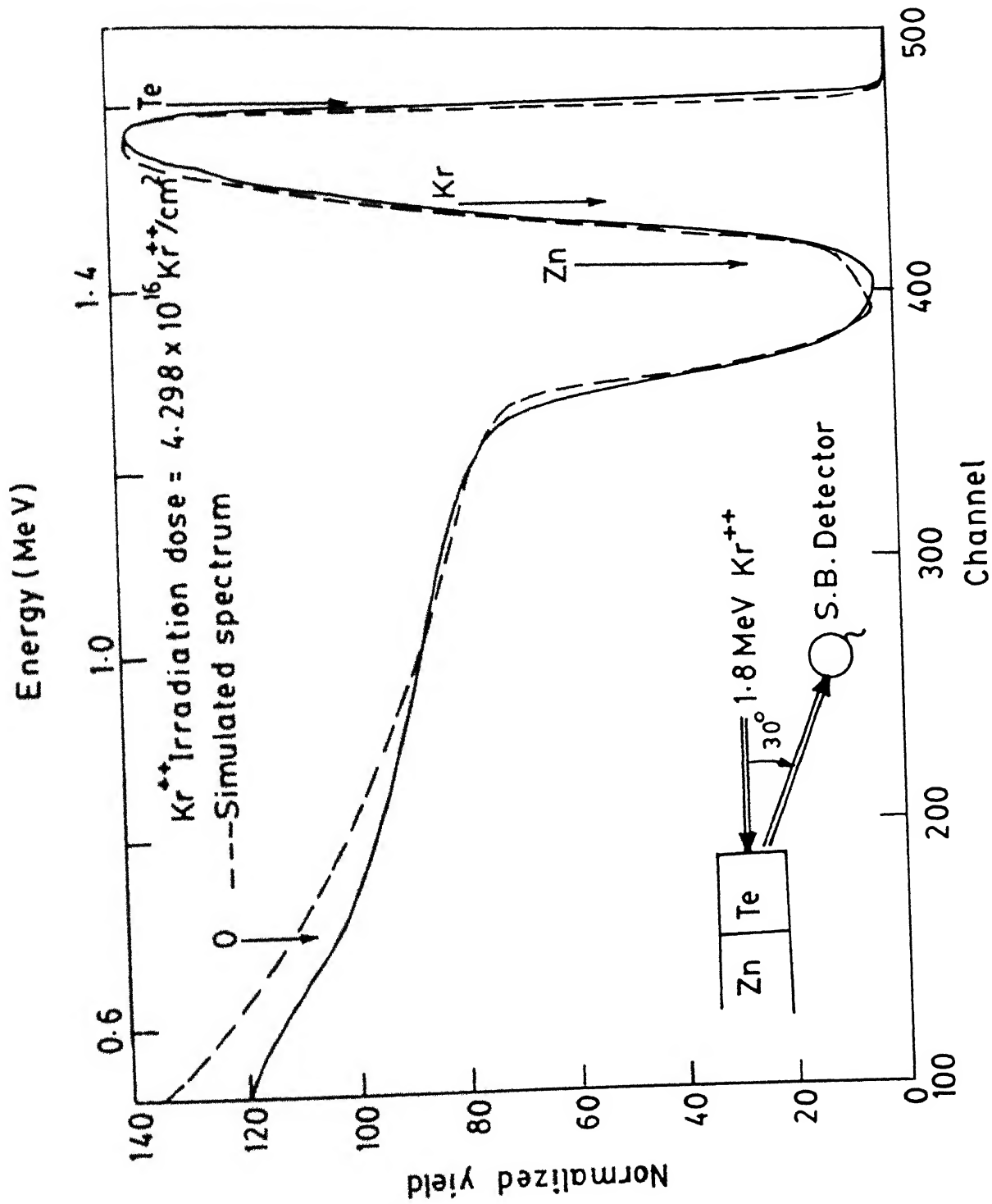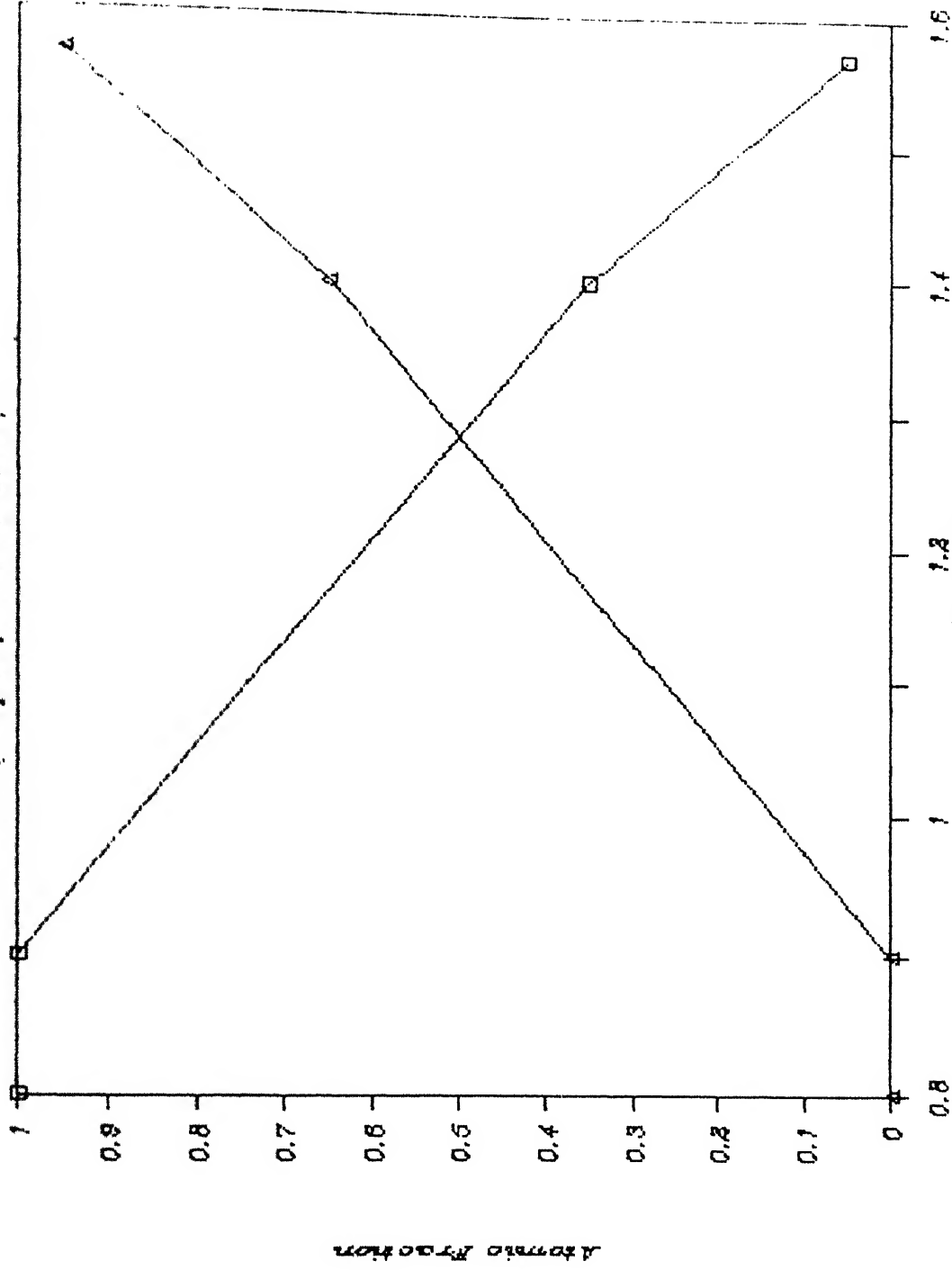
□ Tellurium   △ Zinc

$\phi = 4 \cdot 298 \times 10^{16} \ Kr^{++} / cm^2$

F.I.G. 3.7 (b)
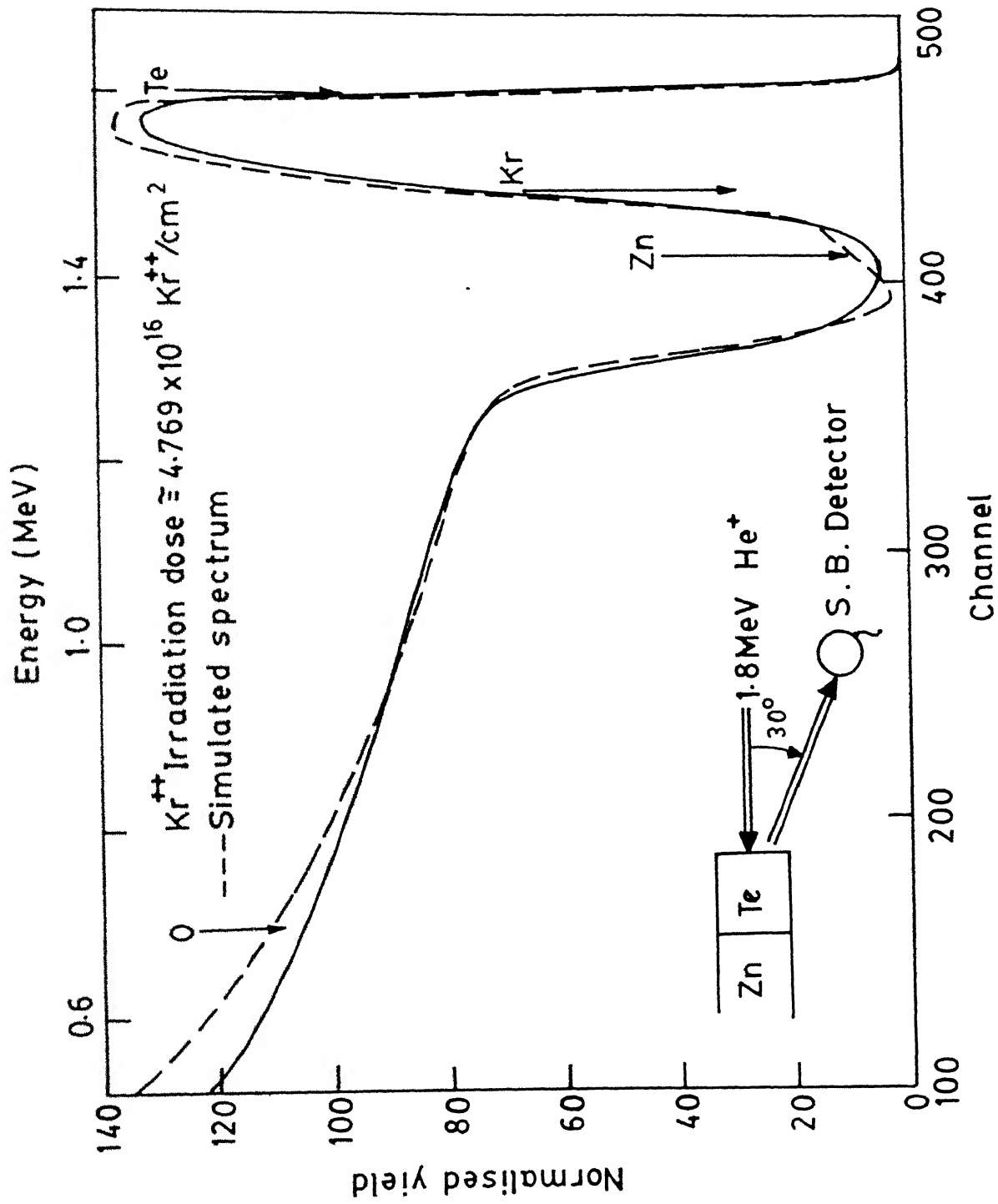
Te & Zn Concentration Profiles
(Input for Simulation)

□ Tellurium   △ Zinc

Depth (Thousands angstroms)

$\Phi = 4.769 \times 10^{16} \; Kr^{++}/cm^2$

FIG. 3.8 (b)

Atomic Fraction

FIG. 3.9

Energy (MeV)

As evaporated sample – Te thickness ~2000 Å
--- Simulated spectrum

Te 1.601 MeV

Kr 1.506 MeV

Zn 1.432 MeV

C 0.4927 MeV
Interface oxygen
O 0.6928 MeV

Normalized yield

Channel

FIG. 3.10

FIG. 3·11 (a)

(input for Simulation)

Atomic fraction

Depth $\left\{ \begin{array}{l} \text{(Thousands)} \\ \text{angstroms} \end{array} \right.$
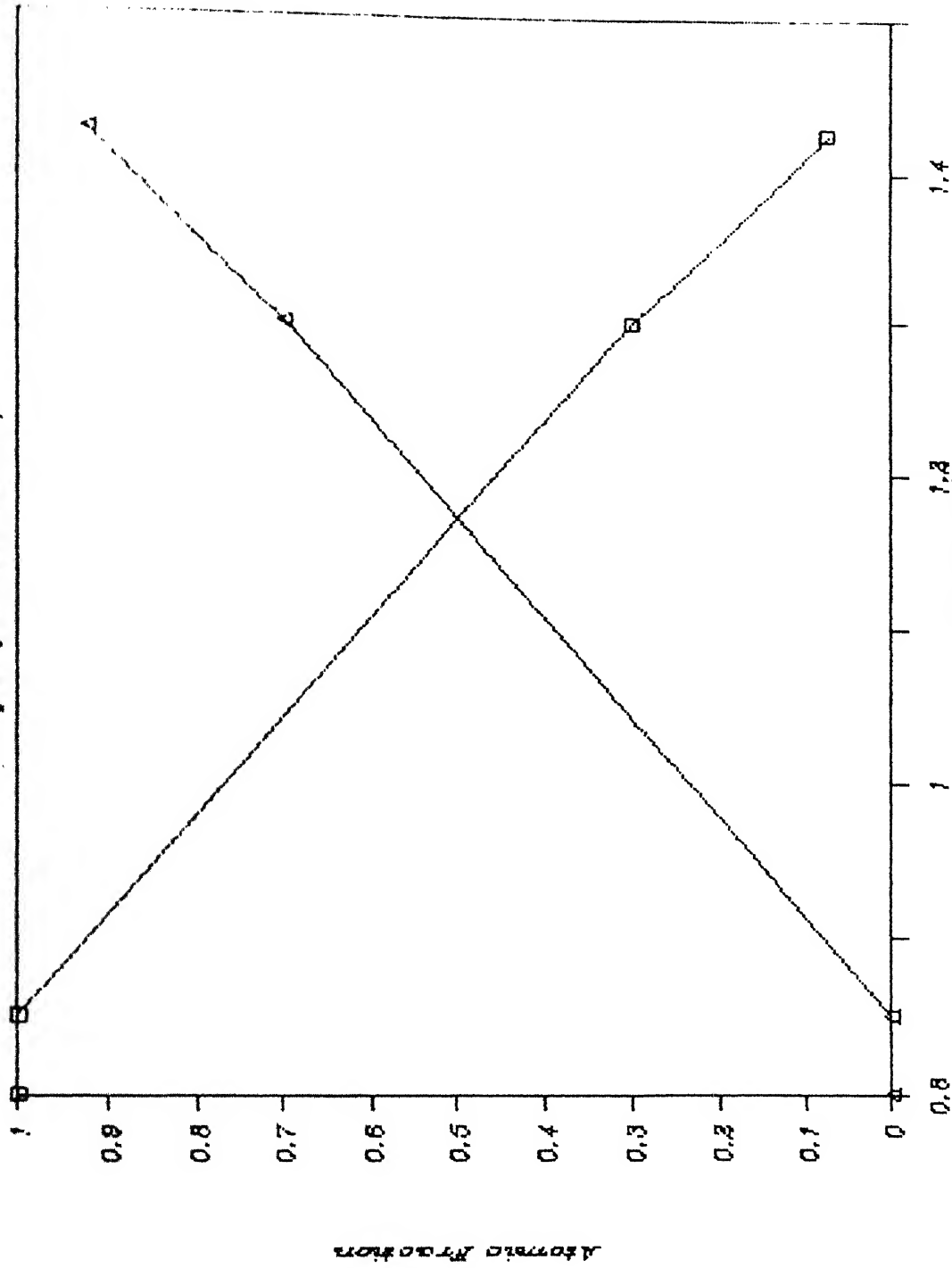
□ Tellurium   △ Zinc
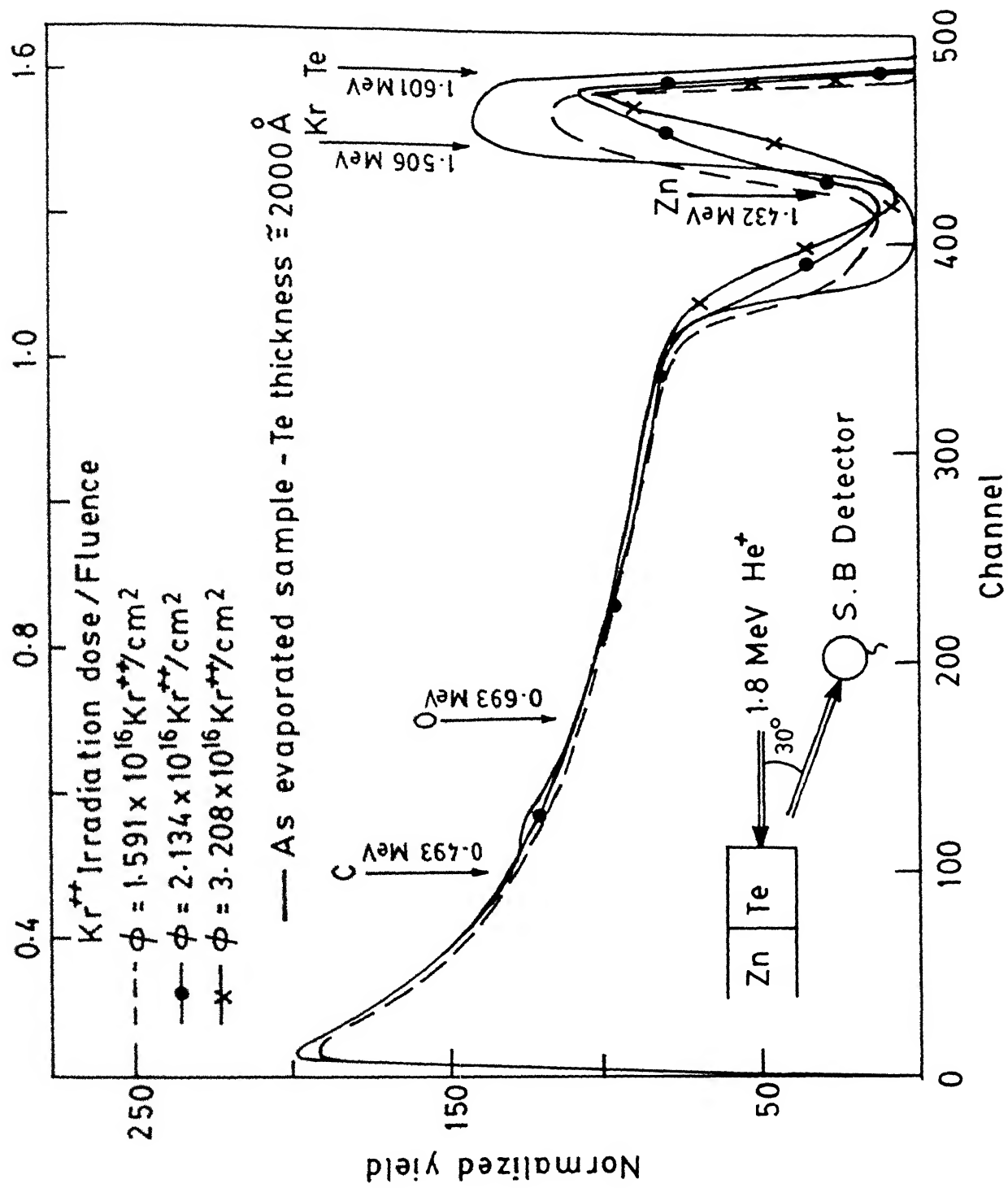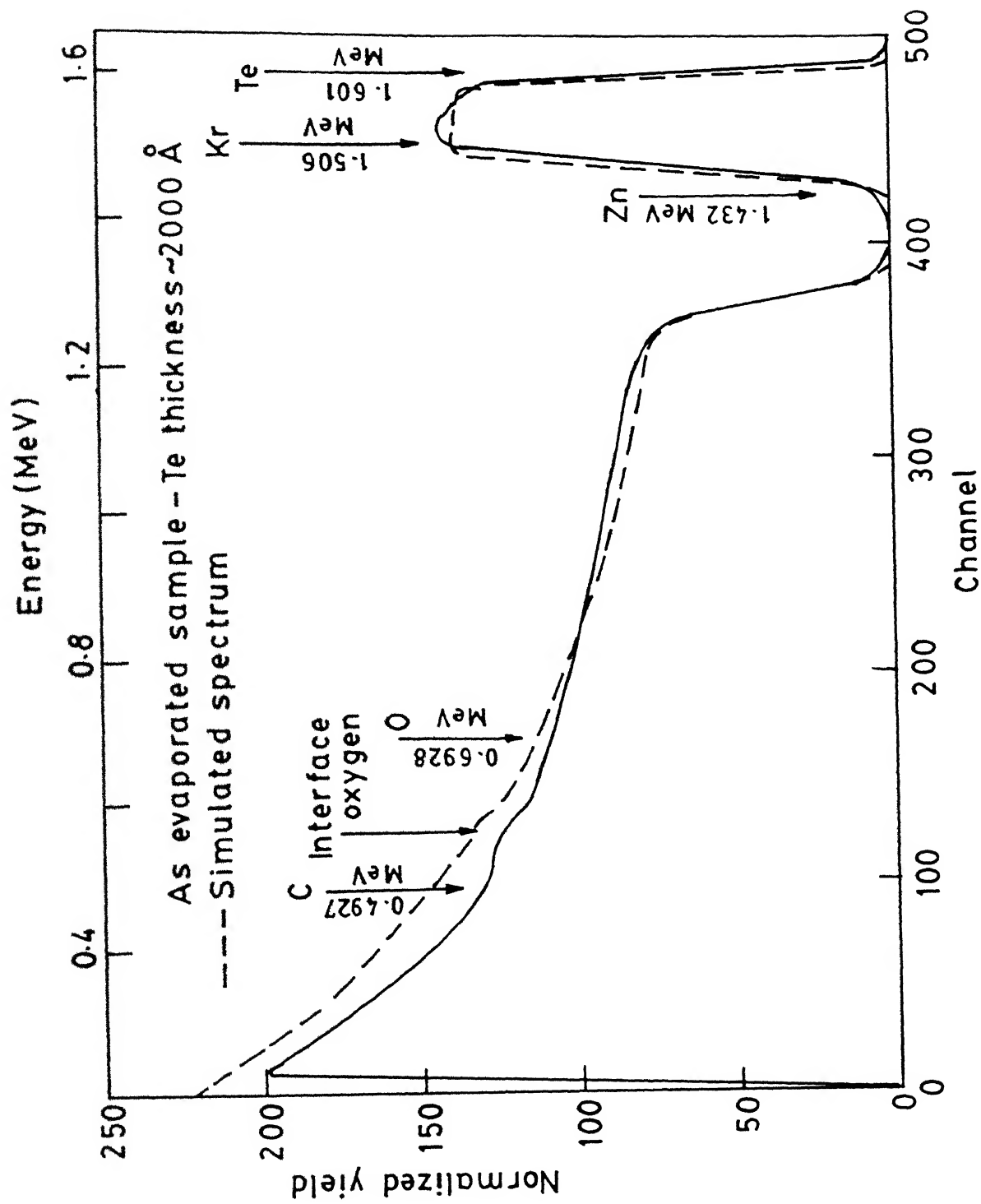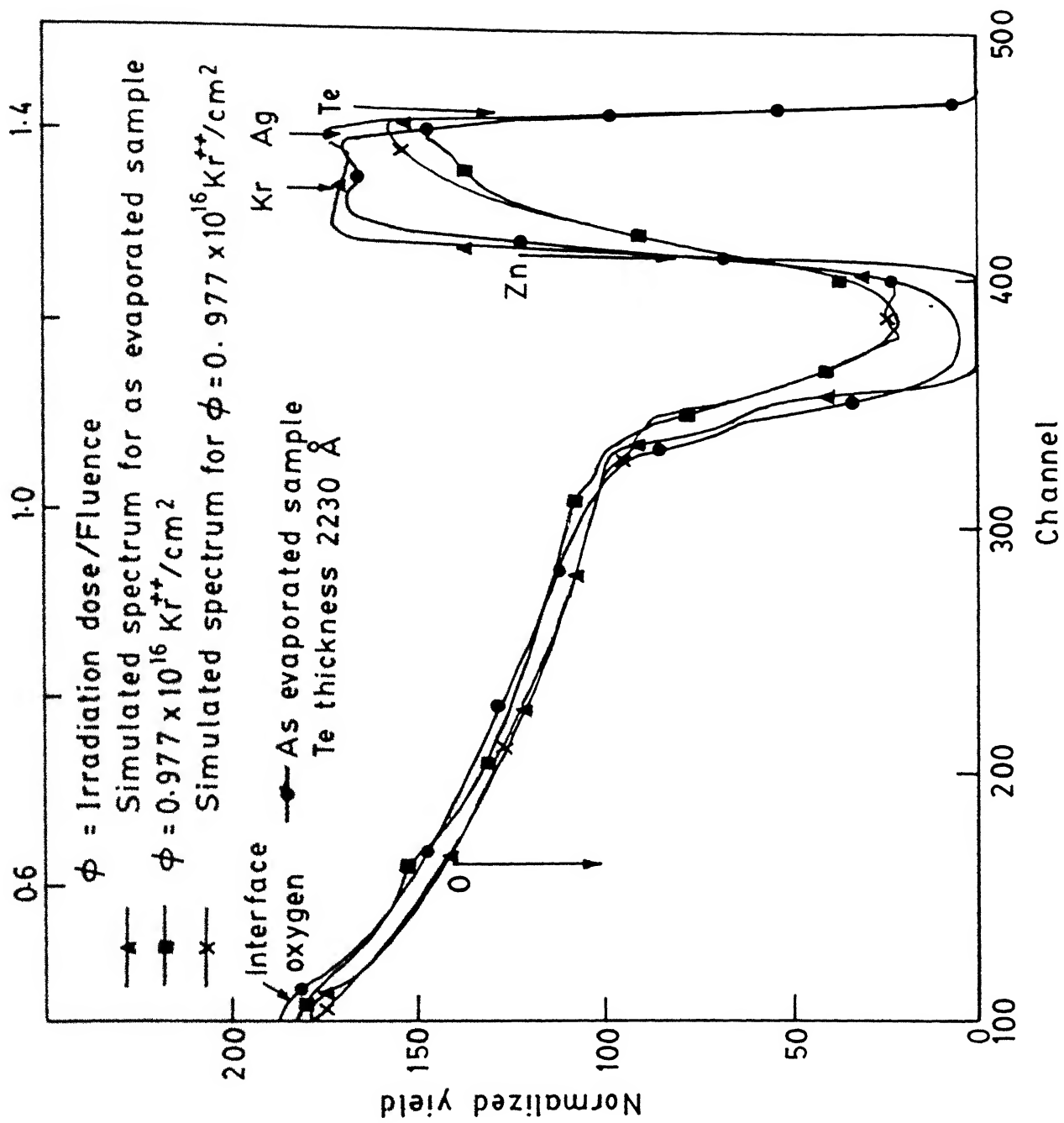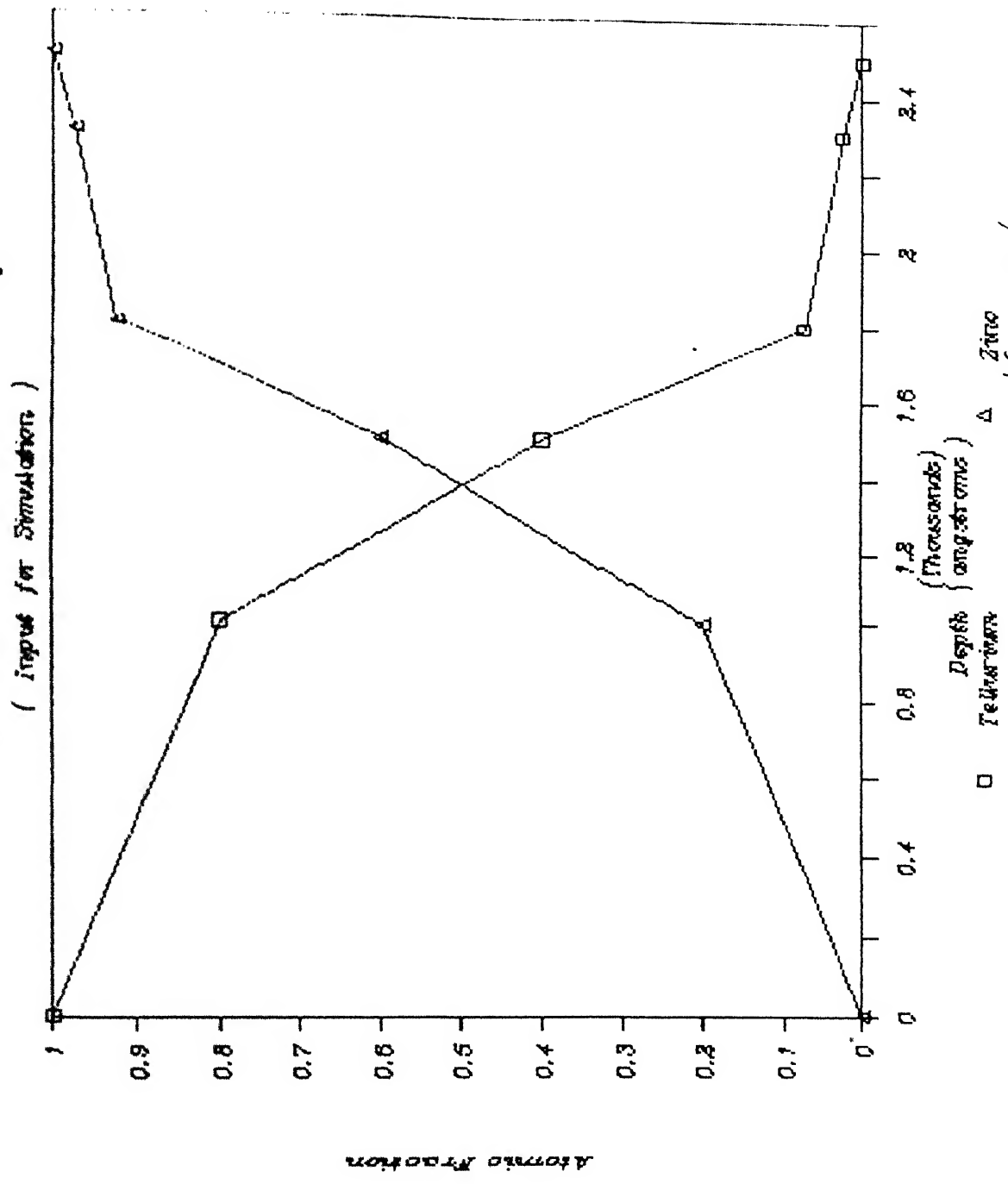
$$\phi = 0.997 \times 10^{16} \; Kr^{++}/Cm^2$$

FIG. 3.11 (b)

FIG. 3.12 (a)

(Input for Simulation)

□ Tellurium △ Zinc

Depth $\left\{\begin{matrix}Thousands\\angstroms\end{matrix}\right\}$

Atomic Fraction
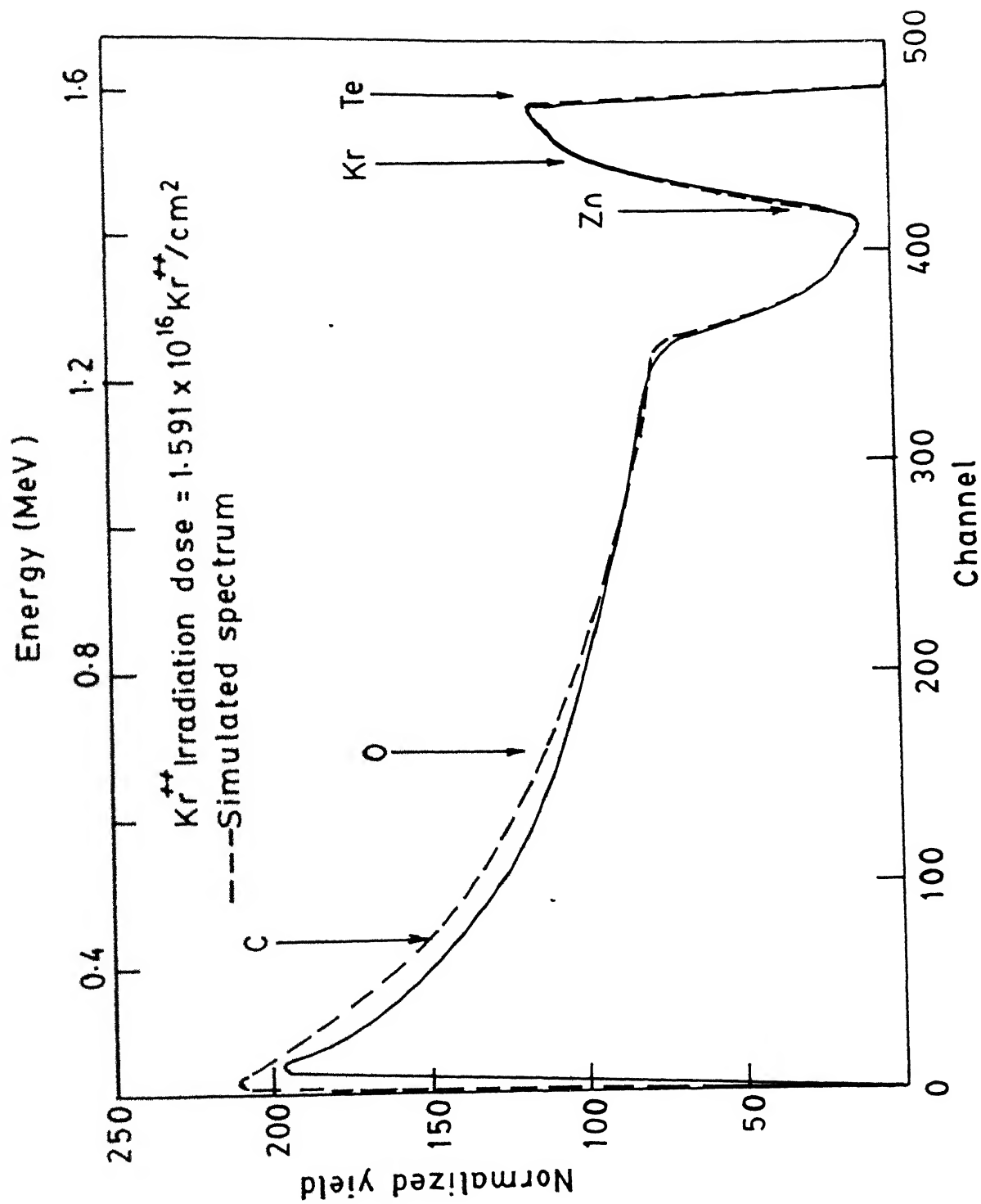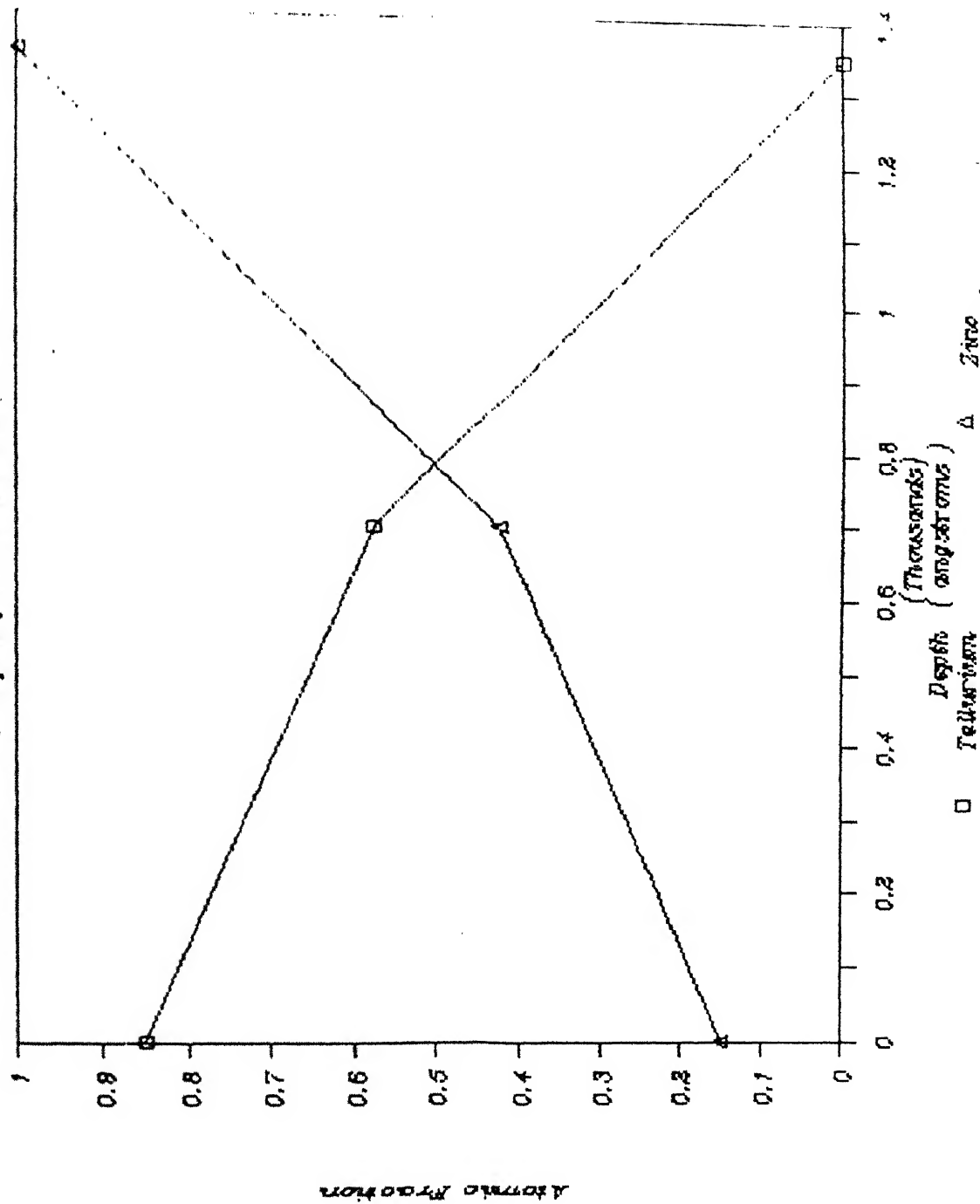
$\Phi = 1.591 \times 10^{16} \ Kr^{++}/cm^2$

FIG. 3.12 (b)
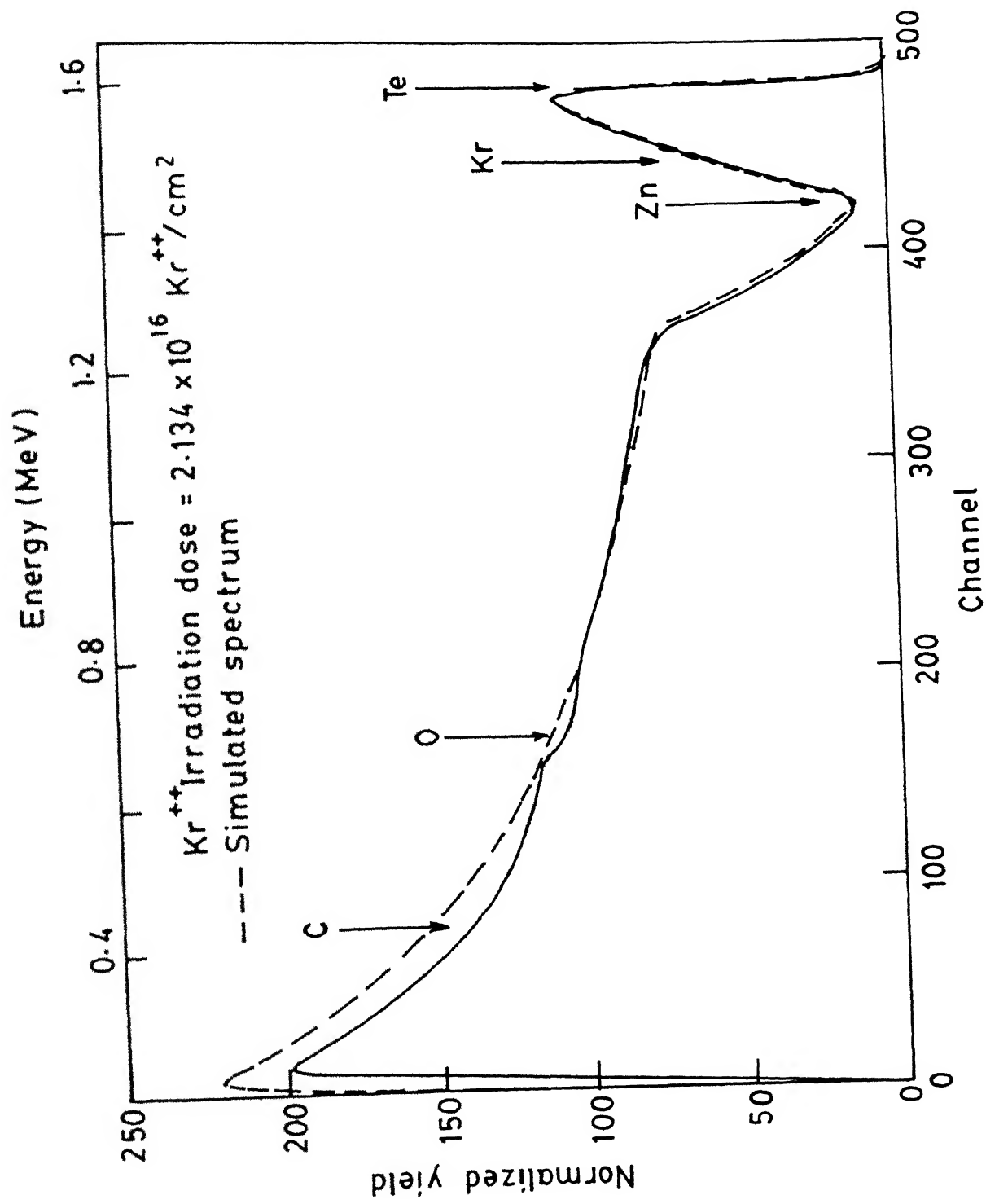
FIG. 3.13 (a)

Te & Zn Concentration Profiles

(Input for Simulation)

Atomic Fraction

□ Tellurium   △ Zinc

Depth (Thousands) (angstroms)
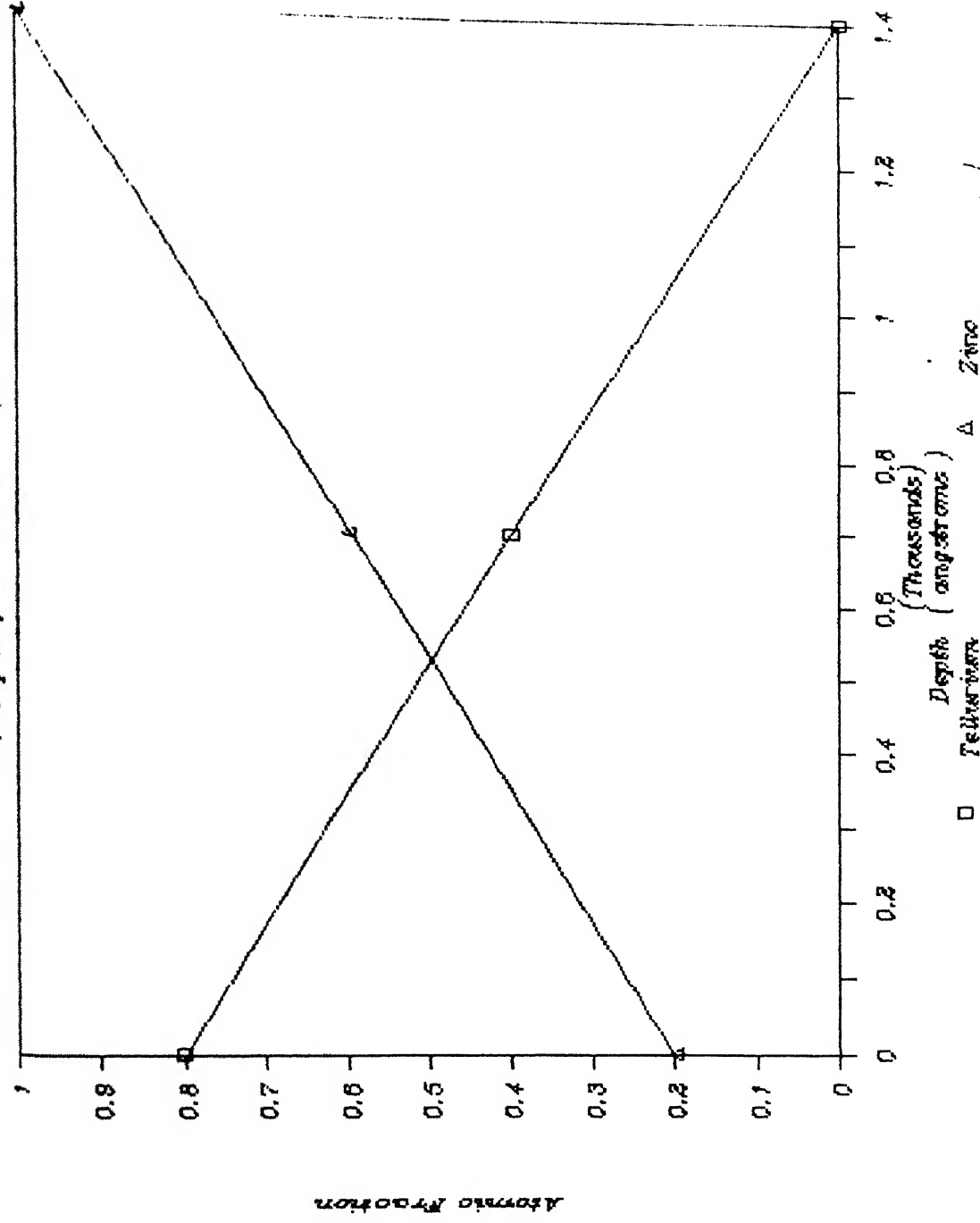
$$\phi = 2 \cdot 134 \times 10^{16} \, K_1^{++}/Cm^2$$

FIG. 3·13 (b)
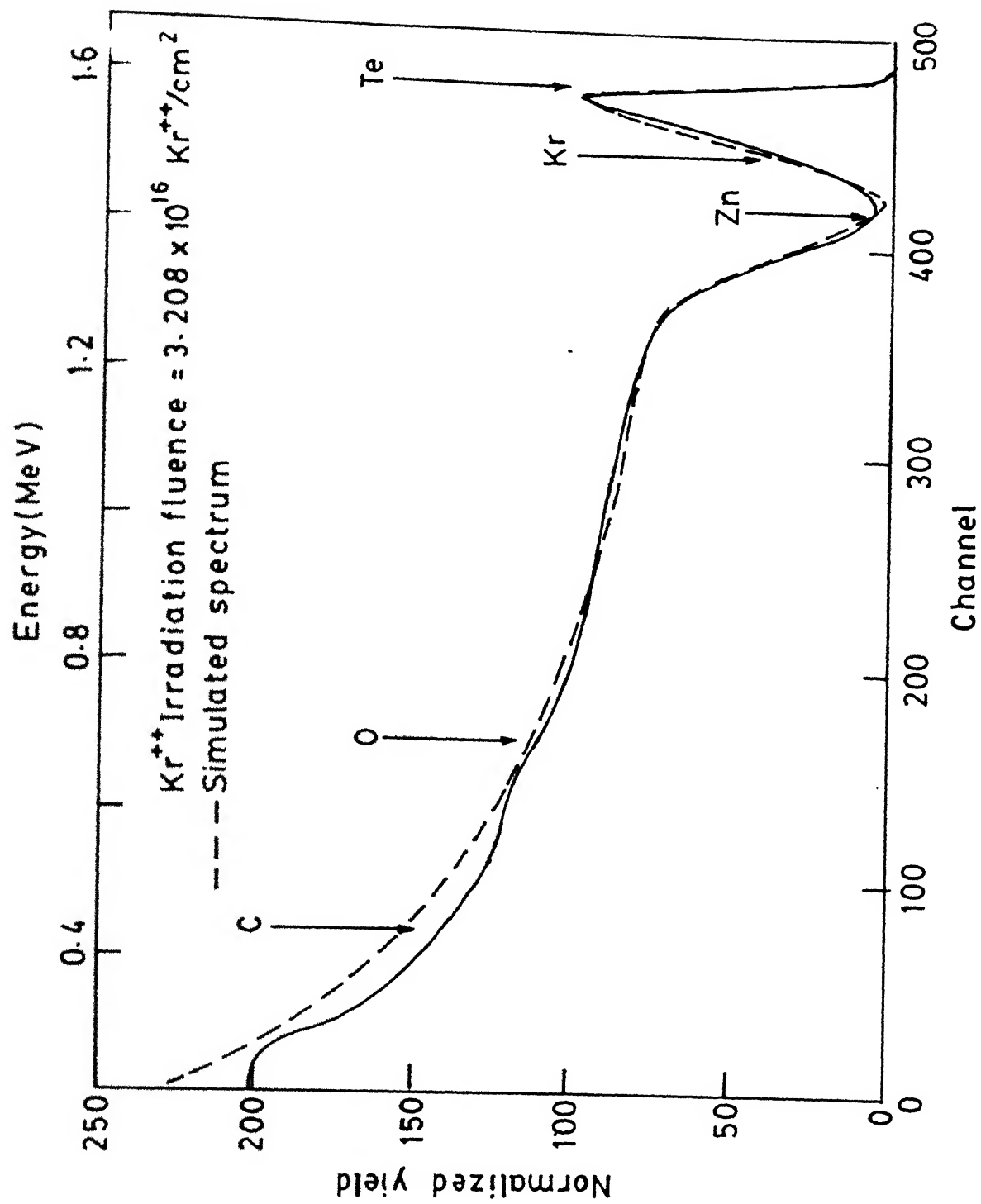
FIG. 3·14 (a)

Te & Zn Concentration Profiles

(Input for Simulation)

$\phi = 3.208 \times 10^{16}$ Kr^{++}/cm^2
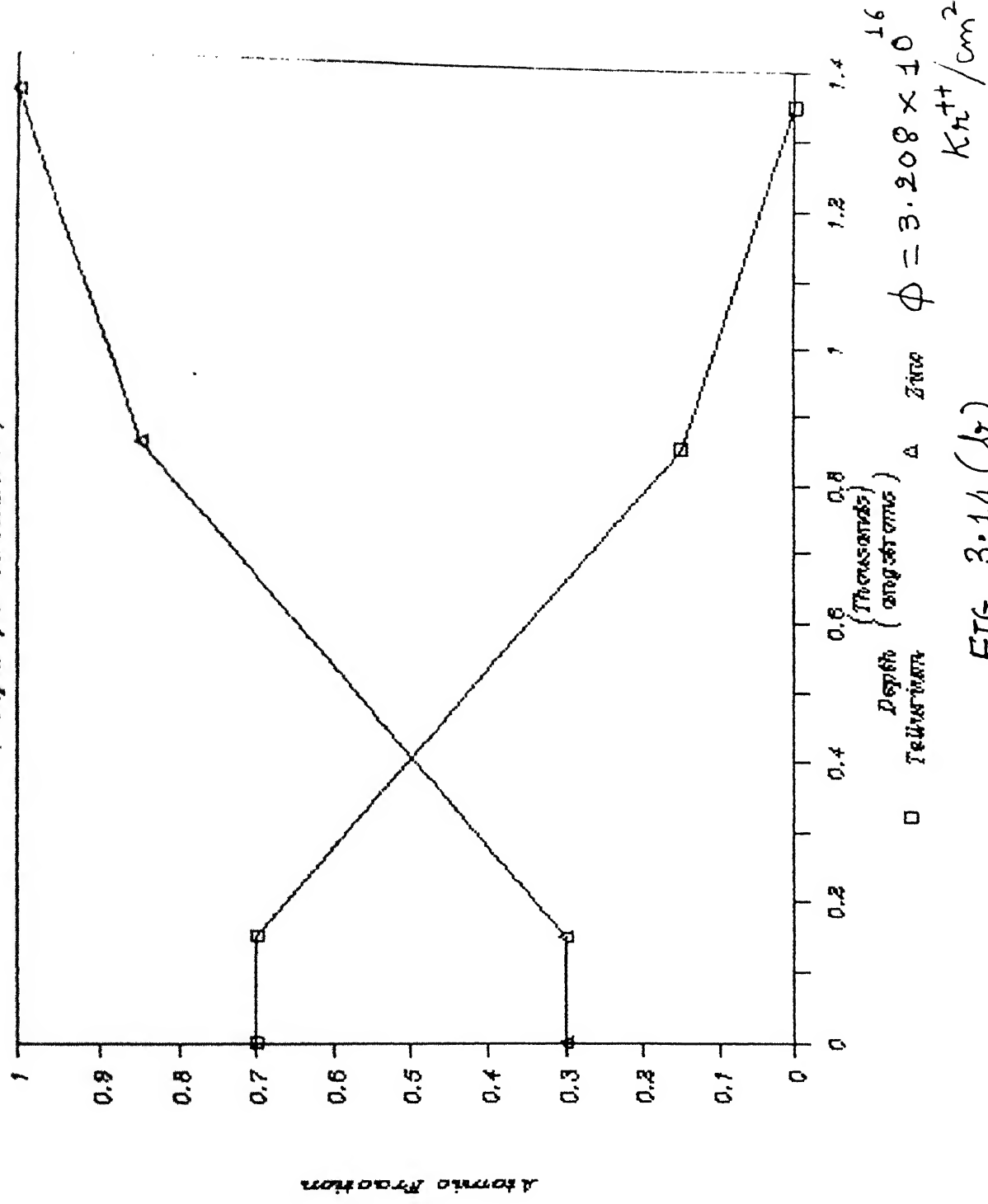
FIG. 3.14 (b)
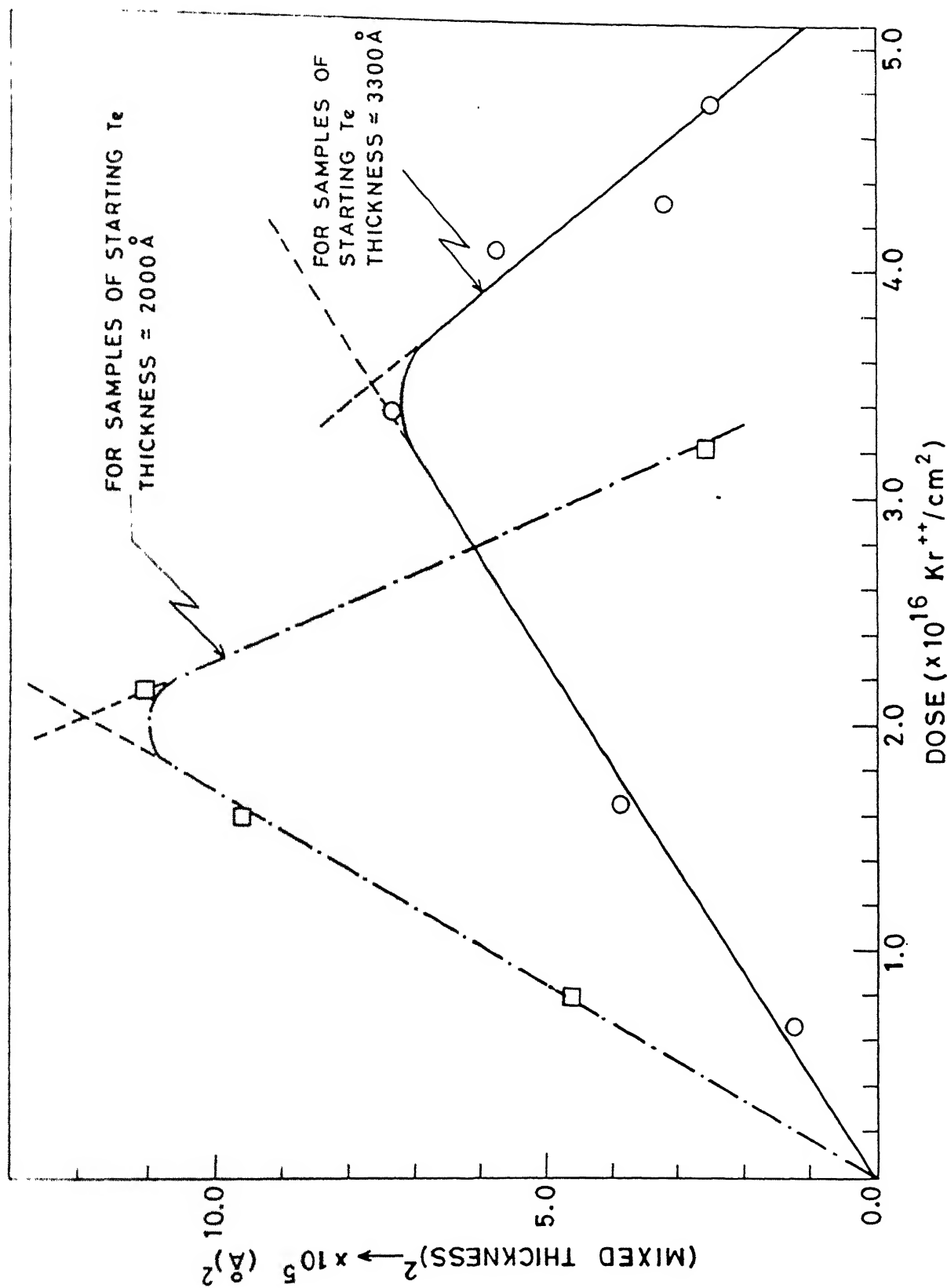
FIG. 3.15 DOSE DEPENDENCE OF ION BEAM MIXING IN Zn/Te

FIG. 3.16

FIG. 3.17

FIG. 3.18

LATERAL STRAGGLE

FIG. 3.19

Command: SB, E, R, P, P, C, N, F2 ....

RECOIL ENERGIES
--- Total ION Energy to Recoils

RECOIL ENERGY (eV / ANGSTROM)

Tellurium

TARGET DEPTH

8400 A

200

100

0

TRIM-88

84 Kr 1000 keV

Ion Number : 2722
Ion Energy : 764 keV

Cascade E = 0 eV
Backscatter: 3
Transmit. = 0

AVERAGES
Mean Range = 3436 A
Straggling = 1238 A
Vac./ Ion = 10271

ENERGY LOSS (%)

	IONS	RECOILS
Ioniz: 27		22.5
Vac. : .5	20	
Phon. : .2	30	

FIG. 3.20

Command: SB, E, R, P, p, L, N, F2 , ...

FIG. 3.21

FIG. 3.22.
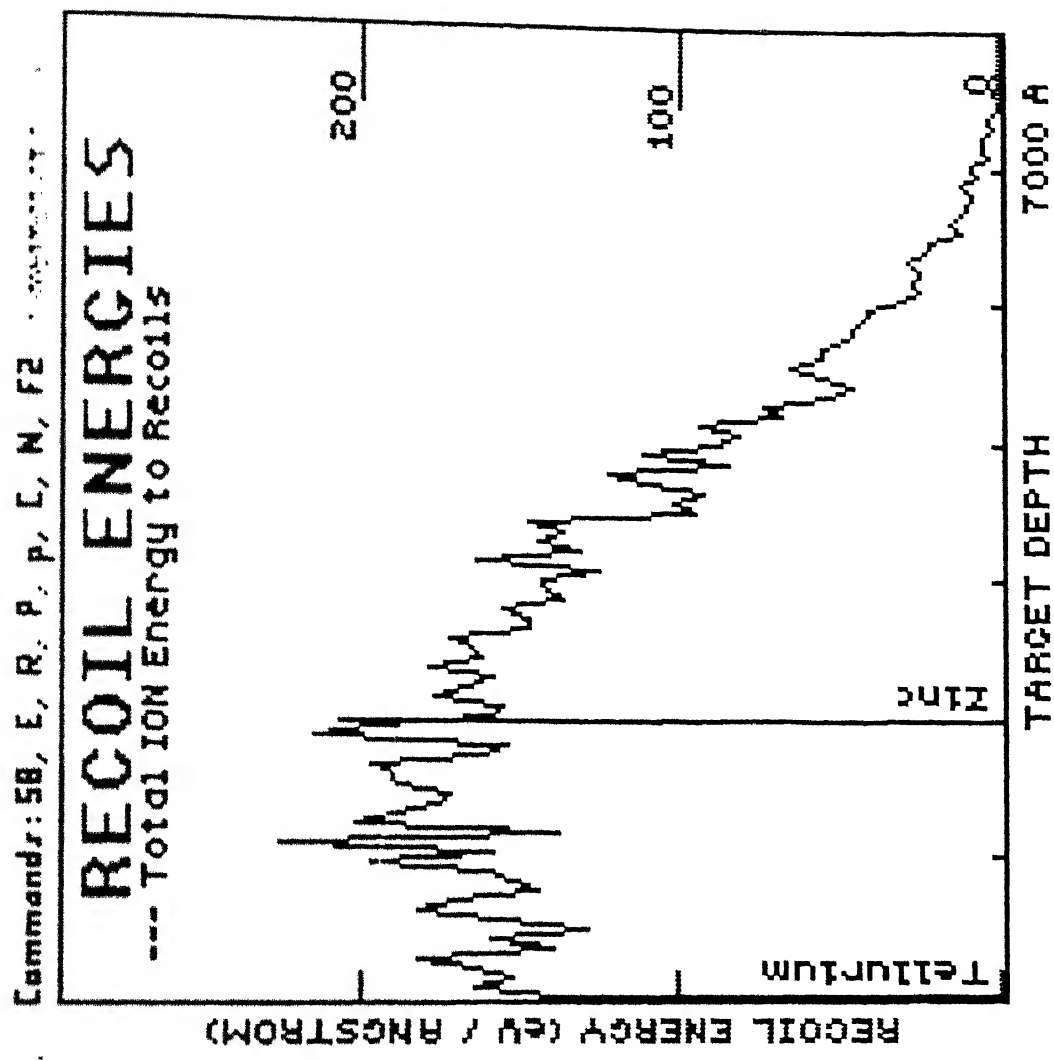
FIG. 3.23
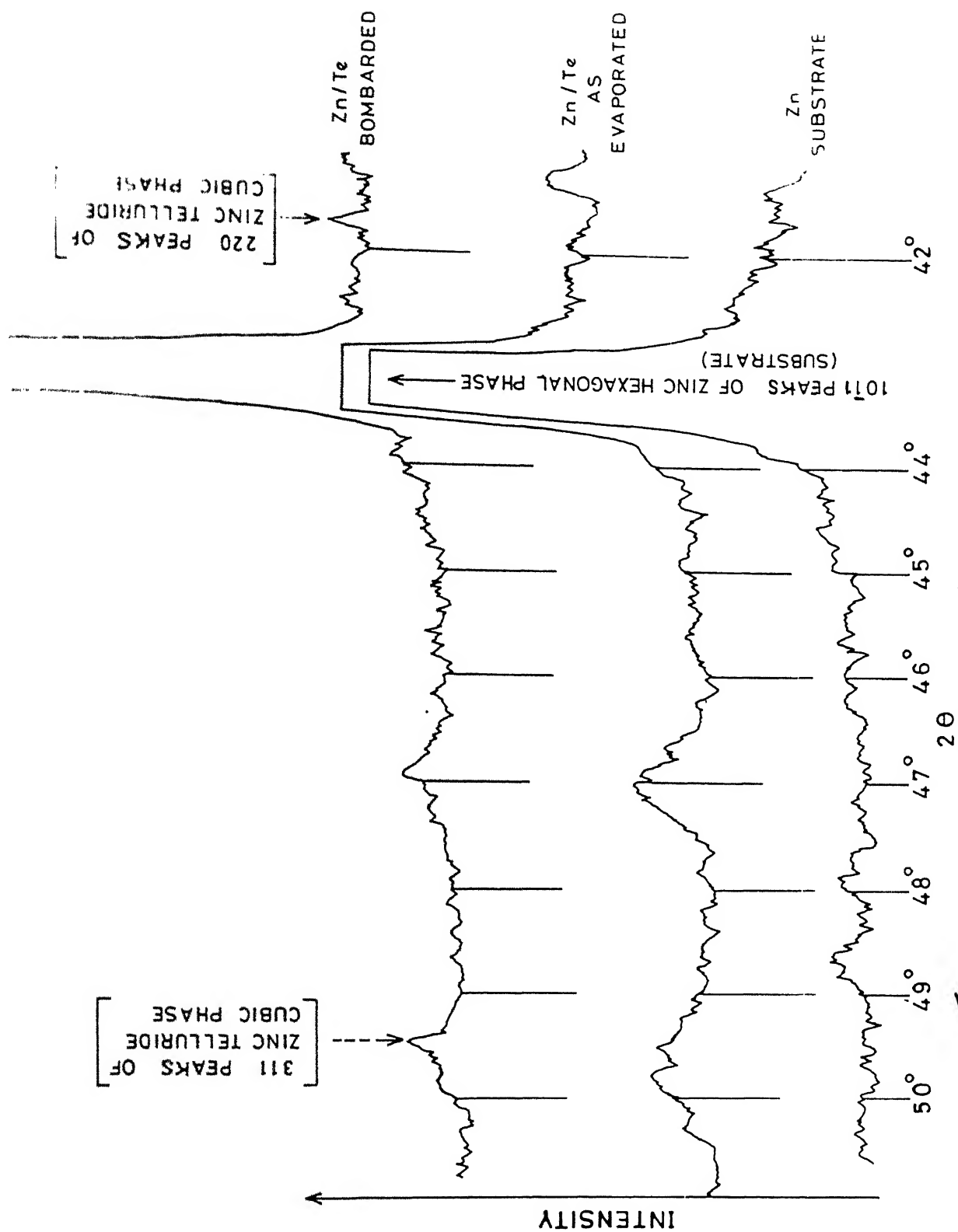
FIG. 3.24

FIG. 3.25

FIG 3.26 X-RAY DIFFRACTION PLOTS FOR THE THICKER Te FILM SAMPLES.
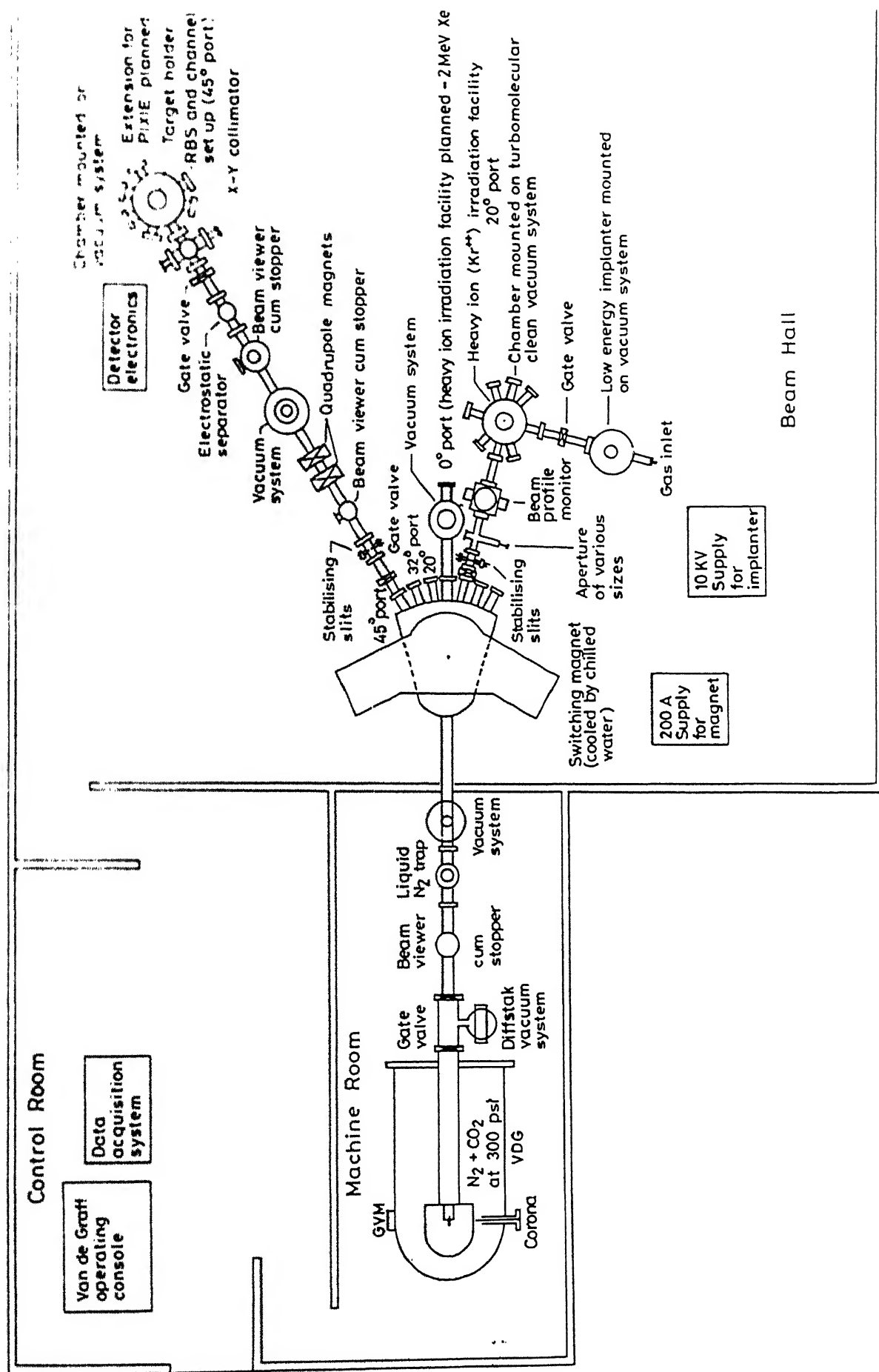
FIG. A1
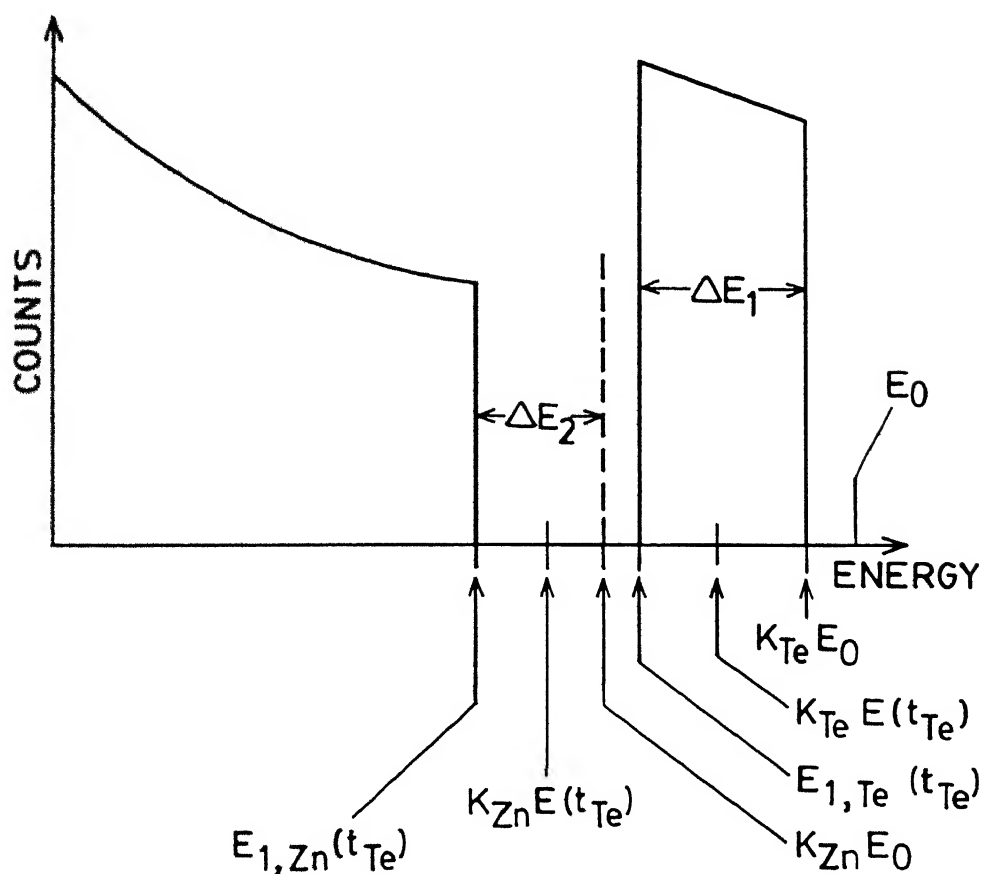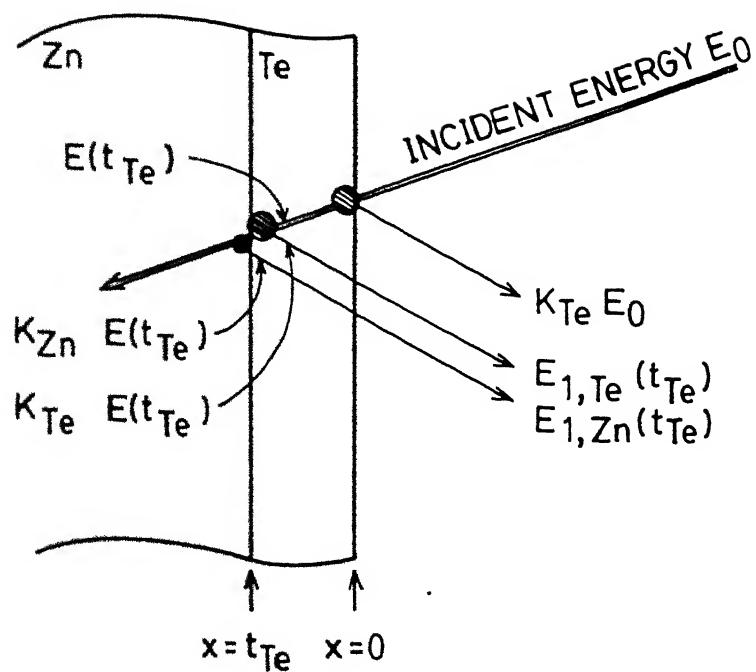
FIG. B1

APPENDIX - A
THE ION BEAM FACILITY

Figure A1 shows the layout of this laboratory. The accelerator is situated in the machine room. The ion beam surface modifications and characterizations are done in the beam hall which also accomodates the switching magnet and its 200 A power supply. The accelerator and the switching magnet are controlled from the control room.

3.2.1   THE VAN DE GRAAFF ACCELERATOR
3.2.1.1   HIGH VOLTAGE GENERATION

The Van de Graaff accelerator generates high voltage on the basis of a very simple principle. If one deposites charge on the inside surface of a closed conducting shell the charge accumulates on the outside surface. Basic electromagnetic laws prevent the charges from residing anywhere inside. Inside the accelerator there exists such a shell which serves as the high voltage terminal. An insulating belt moves through this shell. Electrons are constantly removed from the belt on the side away from the high voltage terminal by applying a positive potential. This leaves a positive charge on the side of the belt moving towards the high voltage terminal. The positive charge on arriving on the inside of the high voltage shell accumulates on its outer surface. Consequently the potential of the high voltage dome/shell rises. If not

properly insulated the dome will lose its charge to the surroundings by sparking. To prevent this the whole assembly is enclosed in a pressure vessel containing an insulating Nitrogen plus CO_2 gas at about 360 psi pressure Figure A1.

Along the length of the accelerator a uniform potential gradient is achieved between the high voltage terminal and ground by a series combination of high value resistors called column resistors. Each column resistor is of approximately 1500 M Ω resistance.

The charge on the high voltage dome is simultaneously and continuously removed by the Corona points shown in Figure A1 and by the series combimation of column resistors. The dome voltage remains fixed when the rate of deposition of charge by the belt equals that of removal by the Corona points and the column resistors.

A generating voltmeter attached on the side of the accelerator pressure vessel measures the dome voltage.

3.2.12. GENERATION OF CHARGED PARTICLE BEAMS

ACCELERATION OF CHARGED PARTICLES

The path followed by the charge particle beams is evacuated to about 5×10^{-6} Torr vacuum. The acceleration of these charged particles occurs in the accelerator tube shown in the Figure. The tube is made up of a series of alternately placed electrodes and insulating glass vertibrae. The connections are made such that one column resistor connects two electrodes of the accelerator tube. Thus there exists an uniform potential gradient inside the tube and the necessary evacuated path. The ions of the required beam are leaked into the accelerating tube from the high voltage side. Under the

potential the charged particles accelerate. The beam so generated is then focused and stabilized.

ION SOURCE, FOCUSING AND BEAM CURRENT CONTROL

The desired ion beam atoms are kept in the form of high pressure gas in gas bottles contained inside the high voltage terminal. A controlled amount of the gas is leaked into an ion source by a mechanism called a thermomechanical leak. In the ion source these gas atoms get ionised on application of a R.F. frequency voltage.

The ions are repelled out of the ion source under the influence of a positive potential applied to an electrode inside the ion source. This positive potential is used to get the desired beam current.

A focusing electrode is mounted just outside the ion source. The voltage applied to this electrode results in proper focusing of the ion beam.

The ion source focusing and beam current controll systems cannot be powered from outside since they are placed inside the high voltage dome. They have to be run on power generated inside the high voltage dome. For the purpose of this power generation two 150 watt alternators are used. These alternators are mounted inside the pulley which supports the charging belt inside the high voltage terminal. The alternators use the belt rotation to generate the necessary power for driving the assembly inside the high voltage shell.

3.2.2 THE SWITCHING MAGNET

The ion beam on emerging from the accelerator is steered into its appropriate ports with the help of a switching magnet. The magnet is shown in Figure A1. Currents of about 100

to 200 amperes are supplied to the magnet by the 200 ampere power supply shown in Figure 3. During operation the magnet is cooled by circulation of chilled deionised water through it.

STEERING OF Kr^{++} BEAM

Singly ionised Kr^+ ions of 1 MeV energy cannot be steered into the 20° port due to the smaller capacity of the magnet. Doubly ionised Kr^{++} ions can be easily steered into the 20° port since the magnet current requirement for Kr^{++} steering is half the current required for Kr^+ steering. The vacuum in the region just before the switching magnet is purposely deteriorated. The Kr^+ ion beam on passing through this region emerges as a Kr^{++} ion beam due to loss of an additional electron per ion. This was the reason why a doubly ionised Kr^{++} beam was used to irradiate the Zn/Te samples.

APPENDIX - B
RUTHERFORD BACKSCATTERING SPECTROMETRY (RBS).

The RBS technique is widely employed for surface analysis of materials especially for thin film study. It is extensively used in the semiconductor industry with no dearth of thin film and ion implantation problems. The next few paragraphs constitute a modest attempt towards describing this important research tool.

B.1   BASIC PHYSICAL CONCEPTS

In a backscattering experiment energetic light ions, such as 1 MeV to 3 MeV protons(^{1}H$^+$) or alpha particles(^{4}He$^+$), are impinged on the sample surface. Some of these backscatter due to collisions with target atoms. The energy of the emergent ^{4}He$^+$ ions depends on the mass of the target atom it has backscattered from and at what depth the collision event has occured. This is due to the difference in recoil energies of ^{4}He$^+$ projectiles colliding with target atoms with differing masses and due to the energy loss process during its passage through the target material. The total number of backscattered alphas detected in a given energy range is dependent on the total number of scatterers (target atoms including impurity atoms) and the likelyhood of occurence of such a scattering event (which results in a ^{4}He$^+$ being scattered into the detector). Further, statistical fluctuations (energy straggling) are inherently present in the energy of the

alpha particles emanating from the sample surface.

These basic physical factors influencing the energy spectrum of the backscattered particles are detailed below.

I)   THE KINEMATIC FACTOR (K) :

The concept of the kinematic factor is intimately linked with the mass resolution capability of RBS. It is a measure of the recoil energy of the projectile of mass M_1 in a collision with an isolated target nucleus of mass M_2 and is defined as

$$K = \frac{E_1}{E_0}$$

(B1).

where E_0 and E_1 are respectively the incident and recoil energies of the projectile in an isolated two body collision with the target atom.

The energy and momentum conservation laws for this two body collison event yield the following expression for the kinematic factor.

$$K = \left[\frac{[1 - X^2 \sin^2\theta]^{1/2} + X \cos\theta}{1 + X} \right]^2$$

(B2).

where $X = \dfrac{M_1}{M_2}$

(B3).

and θ is the scattering angle.

From (B1) one gets the following expression.

$$\Delta E_1 = E_0 \cdot \left(\frac{dK}{dM_2} \right) \cdot \Delta M_2$$

(B4)

projectiles backscattered from target atoms with their masses separated by ΔM_2 .

For a fixed projectile (fixed M_1) a change ΔM_2 results in the largest change in ΔE_1 for scattering angles close to 180°.

For $\theta = \Pi - \delta$ (δ being small) Equation B4 reduces to

$$\Delta E_1 = E_0 \cdot \left[\frac{(1 - X)}{(1 + X)^3} \cdot \left(4(1 + X \delta^2) - \delta^2(1 - X^2) \right) \cdot \frac{M_1}{M_2^2} \right] \cdot \Delta M_2$$

(B5).

Therefore in order to obtain good mass resolution (i.e. to obtain maximum ΔE_1 for a particular ΔM_2) one must use a larger incident energy E_0 (provided E_0 is larger than the binding energy of the atoms to the target and lower than the limit beyond which nuclear reactions get activated), select M_1 to be as close to M_2 as possible provided $M_1 < M_2$ (Figure), make the scattering angle as close to 180° as possible.

One further observes that mass resolution of RBS is intrinsically better for lighter target atoms (small M_2).

II) THE SCATTERING CROSS SECTION (σ)

The differential scattering cross section denoted by $d\sigma/d\Omega$ is defined as

$$\left(\frac{d\sigma}{d\Omega} \right) = \frac{1}{N t} \cdot \frac{1}{Q} \cdot \left(\frac{dQ}{d\Omega} \right)$$

(B6).

where $N t$ is the total areal density (number of atoms per unit area) seen by the incident $^4He^+$ beam, N is the total number of target atoms per unit volume, Q is the total number of $^4He^+$ projectiles incident on the target during RBS analysis

and ω is the solid angle subtended by the detector at the analysis spot on the target.

The quantity dQ/Q is the probability of occurence of a collision between the projectile and the target atom resulting in the scattering of the projectile into the detector solid angle $d\Omega$ situated at the scattering angle θ .

The expression given below for the differential scattering cross section is called Rutherford's formula.

$$\left(\frac{d\sigma}{d\Omega}\right) = \left(\frac{Z_1 \cdot Z_2 \cdot e^2}{4\,E}\right)^2 \cdot \frac{4}{\sin^4 \theta} \cdot \frac{\left(\left[\,1 - x^2\,\sin^2\theta\,\right]^{1/2} + \cos\theta\,\right)^2}{\left[\,1 - x^2\,\sin^2\theta\,\right]^{1/2}}$$

(B7).

The validity of this expression lies in the domain where the distance of closest approach of the projectile and the target nucleus is large compared with the nuclear dimensions but small compared with the Bohr radius $a_0 = \hbar\,/\,m_e \cdot e = 0.53\ \mathring{A}$.

If one considers a detector of finite solid angle Ω then the probability of a successful scattering event is described by the integral scattering cross section defined by

$$\Sigma = \int_\Omega \left(\frac{d\sigma}{d\Omega}\right)\,d\Omega$$

(B8).

The typical values of the detector solid angles are normally of the order of a few millisteradians. The average differential scattering cross section is defined as

$$\sigma = \frac{\Sigma}{\Omega}$$

(B9).

and for small detector solid angles Ω, which one encounters in most RBS set-ups, $\sigma \longrightarrow d\sigma/d\Omega$. Thus for our purpose $d\sigma/d\Omega$ and σ are interchangeable. Thus for the situation with small Ω equation $B6$ reduces to

$$A = \sigma \cdot \Omega \cdot Q \cdot N t$$

The scattering cross section is proportional to z_1^2, inversely proportional to the square of the projectile energy and roughly inversely proportional to the fourth power of Sin $(\theta/2)$. The optimmum parameters must be chosen accordingly.

It should be noted that many of the conditions for maximization of respectively the kinematic factor and the scattering cross section compete with each other and therefore some compromise has to be made in choosing these parameters.

III) THE STOPPING CROSS SECTION

The stopping cross section ε is defined as

$$\varepsilon = \frac{1}{N}\left(\frac{dE}{dx}\right)$$

(B11).

N being the number of target atoms per unit volume and dE/dx is the rate at which energy is lost by the projectile as it moves through the target material. can be fatorised as

$$\varepsilon = \varepsilon_n + \varepsilon_e$$

(B12).

The term ε_n is due to the energy loss due to collisions with the nuclei of target atoms while ε_e is the contribution due to the more continuous energy loss of the projectile to the electrons in the target.

For cases in which atoms in the target exists in the form of molecules of the type $A_m B_n$ (i.e. consisting of m atoms of element A and n atoms of element B), the molecular stopping cross sections can be expressed as

$$\varepsilon^{AB} = (m\,\varepsilon^A + n\,\varepsilon^B)$$

(B13).

ε^A and ε^B are the stopping cross sections for the elemental

targets of A and B atoms respectively. This relation is called the "principle of additivity of stoppint cross sections" or "Bragg's Rule."

As far as theoretical models for estimation of ε are concerned only the simplest classical ones exist. These calculations are extremely difficult to perform. Thus in this area one has faith only in the semiempirical compilations available in the literature.

IV) ENERGY STRAGGLING   .

The projectiles moving through matter lose energy due to ineractions with the individual nuclei as well as with the electron clouds. The energy loss through collisions with the nuclei are violent and discrete. The are statistical fluctuations associated with such a process. Therefore particles incident on a thin slice of thickness ΔX of the target material will emerge out, on passing through ΔX, with differing energies. These statistical fluctuations in the energy of the backscattered particles is referred to as energy straggling. Straggling leads to an impairment of mass and depth resolution of RBS.

B3 > RBS SPECTRUM FOR THE ZN/TE SAMPLES

The backscattering spectrum for a Zn/Te as evaporated sample is shown in Figure B1. The incident beam has energy E_0. The particles backscattered from the surface tellurium atoms will have a slightly reduced energy of $K_{Te} \cdot E_0$. The remaining beam travels through the tellurium film of thickness t_{Te} and appears at the Zn–Te interface with energy

MSP-1991-M-PRA-STU